

THREE-DIMENSIONAL SIMULATIONS OF KELVIN–HELMHOLTZ INSTABILITY IN SETTLED DUST LAYERS IN PROTOPLANETARY DISKS

JOSEPH A. BARRANCO

Department of Physics & Astronomy, San Francisco State University, 1600 Holloway Avenue, San Francisco, CA 94132, USA; barranco@stars.sfsu.edu
Received 2007 November 12; accepted 2008 September 22; published 2009 January 28

ABSTRACT

As dust settles in a protoplanetary disk, a vertical shear develops because the dust-rich gas in the midplane orbits at a rate closer to true Keplerian than the slower-moving dust-depleted gas above and below. A classical analysis (neglecting the Coriolis force and differential rotation) predicts that Kelvin–Helmholtz instability occurs when the Richardson number of the stratified shear flow is below roughly one-quarter. However, earlier numerical studies showed that the Coriolis force makes layers more unstable, whereas horizontal shear may stabilize the layers. Simulations with a three-dimensional spectral code were used to investigate these opposing influences on the instability in order to resolve whether such layers can ever reach the dense enough conditions for the onset of gravitational instability. I confirm that the Coriolis force, in the absence of radial shear, does indeed make dust layers more unstable, however the instability sets in at high spatial wavenumber for thicker layers. When radial shear is introduced, the onset of instability depends on the amplitude of perturbations: small amplitude perturbations are sheared to high wavenumber where further growth is damped; whereas larger amplitude perturbations grow to magnitudes that disrupt the dust layer. However, this critical amplitude decreases sharply for thinner, more unstable layers. In three-dimensional simulations of unstable layers, turbulence mixes the dust and gas, creating thicker, more stable layers. I find that layers with minimum Richardson numbers in the approximate range 0.2–0.4 are stable in simulations with horizontal shear.

Key words: accretion, accretion disks – hydrodynamics – instabilities – methods: numerical – planetary systems: formation – planetary systems: protoplanetary disks

Online-only material: color figures

1. INTRODUCTION

It is a remarkable fact that planets start out as microscopic grains within the protoplanetary disks of gas and dust in orbit around newly formed protostars, somehow growing roughly 10^{40} orders of magnitude in mass in a period no more than 10^7 years corresponding to disk lifetimes (Lissauer 1993). There is no one physical process that can explain growth over this enormous range of sizes: the very smallest grains (micron to millimeter sizes) can grow via collisional agglomeration in which the sticking mechanism is electrostatic in nature; whereas, on the other end of the size spectrum, objects in the kilometer to tens of kilometers regime can grow via gravity-enhanced collisions (Beckwith et al. 2000). The least understood stage of growth is how millimeter-size particles grow to kilometer size; grains in this regime are too large for sticking via electrostatic forces, yet far too small to have any significant self-gravity. Even more problematic is the fact that particles in this intermediate-size regime are strongly affected by aerodynamic drag of the surrounding gas: meter-size objects, for example, have radial drift speeds on the order of 10^4 cm s⁻¹ at 1 AU and thus spiral inward onto the protostar on the timescale of a few hundred years (Weidenschilling 1977). Whatever process is responsible for grain growth through this range of sizes must act on timescales faster than this inspiral time if any raw materials are to be available to build protoplanets.

Goldreich & Ward (1973) and Safronov (1969) proposed that a very thin, very dense sheet of settled dust in the midplane of the protoplanetary disk might be gravitationally unstable; the nonlinear evolution would result in the layer clumping-up directly into gravitationally bound kilometer-size planetesimals on a timescale of order the orbital period. According to this

scenario, there is a direct jump from small particles to kilometer-size planetesimals without growing slowly through the intermediate sizes which have very short orbital decay timescales. As attractive as this mechanism is for planetesimal formation, a significant obstacle is turbulence which can stir and mix the dust with the gas and prevent the dust layer from settling into a thin enough, dense enough sheet for the gravitational instability to operate (Weidenschilling 1980).

Even in the absence of any mechanism to drive turbulence, the settling of the dust particles into a thin sublayer in an initially laminar midplane would create a vertical shear that might be unstable to Kelvin–Helmholtz instability. Because of a relatively weak outward radial pressure gradient, pure gas in a protoplanetary disk orbits the protostar at a rate slightly slower than true Keplerian: $V_{\text{gas}} = V_K(1 - \eta)$, where $\eta \sim 10^{-3}$ for typical conditions at 1 AU (Adachi et al. 1976; Weidenschilling 1977). Pure dust, in the absence of any gas, would orbit exactly at the Keplerian rate. One can show that in the limit of perfect dust–gas coupling, the orbital velocity of a mixture of gas and dust is a function of the local dust-to-gas ratio (Adachi et al. 1976); as dust settles into the midplane, the dust-rich gas in the midplane orbits faster than the dust-depleted gas above and below the midplane. Two-fluid (gas and dust) numerical simulations by Cuzzi et al. (1993), Champney et al. (1995), and Dobrovolskis et al. (1999) suggested that turbulent diffusion would prevent settling of grains into thin enough sheets for gravitational instability.

The onset of Kelvin–Helmholtz instability is determined by a competition between the stabilizing effects of stratification and the destabilizing effects of vertical shear. If there is no rotation and no horizontal shear, then a necessary (but not sufficient) condition for instability is the Richardson number criterion

(Chandrasekhar 1960; Drazin & Reid 1981):

$$Ri(z) \equiv \frac{N^2}{(dU/dz)^2} < Ri_{\text{crit}} \sim 0.25 \quad \text{for some } z, \quad (1)$$

where N is the Brunt–Väisälä frequency (the frequency of buoyant oscillations of a stably-stratified medium) and dU/dz is the vertical shear. The critical Richardson number of one-quarter corresponds to a state in which the kinetic energy of the vertical shear is sufficient to lift the heavier gas out of the gravitationally potential well and remix it with the lighter overlying fluid. Assuming that dust would settle into thinner and thinner layers down to the limit set by the classic Richardson criterion, Sekiya (1998); Sekiya & Ishitsu (2000), and Youdin & Shu (2002) determined critical vertical quasi-equilibrium dust profiles and investigated the conditions necessary for such layers to be gravitationally unstable. Garaud & Lin (2004) pursued two-fluid linear calculations (without rotation and radial shear) of dust sedimentation into sheets and found that the Kelvin–Helmholtz instability was excited before gravitational instability unless the global dust-to-gas ratio was greatly enhanced over solar abundance. Youdin & Chiang (2004) suggested that such enhancements might be attainable because the inward drift speed decreases as particles migrate inward, resulting in “particle pile-ups.”

It is not at all clear whether the classic Richardson number criterion is appropriate for the Kelvin–Helmholtz instability in protoplanetary disks in which both rotation and radial shear could significantly affect the onset of instability as well as alter the nonlinear evolution of any instability that develops. Ishitsu & Sekiya (2003) pursued a purely linear analysis to study the effect of radial shear on the time evolution of unstable Kelvin–Helmholtz modes and showed that the modes were sheared to higher spatial wavenumber and could eventually be stabilized. On the other hand, Gomez & Ostriker (2005) investigated the effects of the Coriolis force on the onset of instability, and found that settled layers were unstable at much higher critical Richardson numbers (corresponding to thicker dust layers) than in the classic case. However, these simulations were two-dimensional and did not include the Keplerian shear. Johansen et al. (2006) performed two-dimensional simulations with Lagrangian particles embedded in the fluid and showed that layers evolved toward a self-regulated state in which further settling was inhibited by turbulence generated by Kelvin–Helmholtz instability, maintaining the layer in a dynamic equilibrium right at the critical thickness for instability. Like Gomez & Ostriker (2005), they found that the dust layers had very high critical Richardson numbers. Surprisingly however, they found the dust was not uniformly mixed in the saturated turbulent state, but was strongly clumped via a mechanism similar to the streaming instability of Youdin & Goodman (2005), which is only present if particles are allowed to slip through the gas. They suggested that such clumps might potentially be gravitationally unstable. Further work by Youdin & Johansen (2007); Johansen & Youdin (2007), and Johansen et al. (2007) have shown that despite Kelvin–Helmholtz instability, large boulders (meter scale) can settle, clump via the streaming instability, and potentially undergo gravitational collapse directly into kilometer-sized planetesimals.

The motivation for this work is to investigate the apparently opposing influences of rotation (destabilizing) and radial shear (stabilizing) on the Kelvin–Helmholtz instability of settled dust layers and resolve whether or not such layers can ever reach the thin enough, dense enough conditions for the onset

of gravitational instability. Apart from the impact of Kelvin–Helmholtz instability on the formation of planetesimals, it is important to determine the vertical distribution of dust in order to correctly interpret observations (Brittain et al. 2005; Rettig et al. 2006; Dullemond et al. 2007). The approach we take here is that the dust is perfectly coupled to the gas; in terms of timescales, the friction or stopping time (see Equation (9)) is much shorter than the evolution of Kelvin–Helmholtz instabilities if they are present. We will not simulate the formation of the dust layer from a well-mixed state, but assume that the layers have already formed with a given profile of the dust-to-gas ratio. If the layer turns out to be unstable on a fast timescale, it implies that such a layer would never have formed in the first place. In Section 2, we present equations for the hydrodynamic evolution of settled dust layers in the limit of perfect dust–gas coupling. In Section 3, we revisit the cases of (1) no rotation, no shear, and (2) rotation, no shear. In Section 4, we present new three-dimensional simulations of the evolution of settled dust layers with both rotation and shear. Finally, in Section 5, we discuss the impact of these results on the planetesimal formation via gravitational instability.

2. SINGLE-FLUID EQUATIONS FOR PERFECTLY COUPLED GAS & DUST IN A THREE-DIMENSIONAL CARTESIAN SHEARING BOX

2.1. Equilibrium for a Gas Disk

Consider the time-independent, axisymmetric azimuthal flow \bar{V}_ϕ of gas around a protostar of mass M_\star

$$\frac{\bar{V}_\phi^2}{r} \hat{\mathbf{r}} = \nabla \Phi + \frac{1}{\bar{\rho}_g} \nabla \bar{p}_g, \quad (2)$$

where (r, ϕ, z) are protostar-centered cylindrical coordinates with corresponding unit vectors $(\hat{\mathbf{r}}, \hat{\boldsymbol{\phi}}, \hat{\mathbf{z}})$, $\Phi = -GM_\star/\sqrt{r^2 + z^2}$ is the gravitational potential, G is the gravitational constant, and $\bar{\rho}_g$ and \bar{p}_g are the equilibrium gas density and pressure. Protoplanetary disks are thermally cool in the sense that the gas sound speed c_s is much slower than the Keplerian orbital velocity $V_K(r) \equiv r\Omega_K(r) \equiv \sqrt{GM_\star/r}$. Hydrostatic balance implies that the time it takes sound waves to traverse the thickness of the disk is on the order of the orbital period; thus, cool disks are geometrically thin (see Frank et al. 1985).

$$c_s \sim \Omega_K H_g, \quad (3a)$$

$$\delta \equiv c_s/V_K \sim H_g/r < 1, \quad (3b)$$

where H_g is the vertical pressure scale height. In cool disks, the radial component of the protostellar gravity nearly balances the centrifugal force, but because of the relatively weak outward radial pressure force, the gas orbits at slightly slower than the Keplerian velocity (Adachi et al. 1976; Weidenschilling 1977)

$$\Omega(r, z) = \Omega_K(r) [1 - \eta(r, z)], \quad (4a)$$

$$\eta(r, z) = \frac{-(\partial \bar{p}_g / \partial r) / \bar{\rho}_g}{2GM_\star/r^2} + \frac{3}{4} \left(\frac{z}{r}\right)^2 + \mathcal{O}(\delta^4), \quad (4b)$$

where the fractional deviation from Keplerian is $\eta \sim \delta^2 \ll 1$. Depending on the disk model, η typically takes values between 10^{-3} and 10^{-2} at $r = 1$ AU, and the Mach number for the maximum deviation from Keplerian is of order $\eta V_K/c_s \sim 0.1$.

In contrast to a pure gas disk which orbits at a slightly sub-Keplerian speed, a disk of pure (pressureless) dust orbits at the full-Keplerian speed. As dust sediments into a thin sheet and creates a vertical shear, we expect that Kelvin–Helmholtz instabilities might potentially develop when the local dust-to-gas ratio $\mu \equiv \rho_d/\bar{\rho}_g$ in the midplane approaches of order unity:

$$\mu_0 \equiv \mu(z=0) \sim 1 \quad \text{when} \quad \lambda \equiv H_d/H_g \sim \Sigma_d/\Sigma_g, \quad (5)$$

where ρ_d is the local mass density of dust, H_d is the scale height of the dust sublayer, Σ_d is the surface mass density of dust, and Σ_g is the surface mass density of gas. When Kelvin–Helmholtz instabilities do develop, the horizontal and vertical scales of the fastest growing unstable modes are typically of order the thickness of the shear layer: $(\Delta r, r\Delta\phi, \Delta z) \sim H_d \sim \lambda H_g$. We can divide the velocity into two components: the velocity across the region of interest due to the Keplerian shear $\tilde{v} \sim H_d\Omega_K \sim \lambda H_g\Omega \sim \lambda c_s$, and the differential velocity between the settled dust sublayer and the dust-depleted gas above and below the midplane $\tilde{v} \sim \eta V_K \sim \delta c_s$. The Mach number of the flow is thus $\epsilon = \max(\delta, \lambda)$.

Motivated by this dimensional analysis, we simulate the dynamics only within a small patch of the disk $(r - r_0, r_0(\phi - \phi_0), z) \rightarrow (x, y, z) \sim H_d \sim \lambda H_g$ that corotates with the gas at some fiducial radius r_0 with angular speed $\Omega_F \equiv \Omega_{K0}(1 - \eta_0)$, where $\Omega_{K0} \equiv \Omega_K(r_0)$ and $\eta_0 \equiv \eta(r_0, z=0)$. The tidal term (i.e., the remainder after the near cancellation of the inward radial protostellar gravity and the outward centrifugal force) and the equilibrium pressure gradient are given by

$$-\frac{\partial\Phi}{\partial r} + \Omega_F^2 r = \Omega_{K0}^2 r_0 [3x/r_0 - 2\eta_0 + \mathcal{O}(\delta^2\lambda^2, \delta^3\lambda, \delta^4)], \quad (6a)$$

$$-\frac{1}{\bar{\rho}_g} \frac{\partial\bar{p}_g}{\partial r} = \Omega_{K0}^2 r_0 [2\eta_0 + \mathcal{O}(\delta^2\lambda^2, \delta^3\lambda)], \quad (6b)$$

$$-\frac{1}{\bar{\rho}_g} \frac{\partial\bar{p}_g}{\partial z} = \Omega_{K0}^2 r_0 [z/r_0 + \mathcal{O}(\delta^2\lambda^2)]. \quad (6c)$$

In this work, we assume the background gas temperature is spatially constant, $\bar{T} = T_0$, so that the gas pressure gradient can be written in terms of the gas-density gradient: $(\nabla\bar{p}_g)/\bar{\rho}_g = \mathcal{R}T_0\nabla\ln\bar{\rho}_g$, where $\mathcal{R} \equiv C_P - C_V$ is the gas constant. The equilibrium gas density is thus

$$\bar{\rho}_g(x, z) = \rho_0 \exp(-x/\Lambda_g - z^2/2H_g^2), \quad (7a)$$

$$H_g^2 \equiv \mathcal{R}T_0/\Omega_{K0}^2, \quad (7b)$$

$$\Lambda_g \equiv \mathcal{R}T_0/2\Omega_{K0}^2\eta_0 r_0 = (c_{s0}/2\eta_0 V_{K0})H_g. \quad (7c)$$

In the simulations presented in this work, we generally ignore the global radial gradient of the background gas density $\Lambda_g \rightarrow \infty$.

2.2. Dynamic Equations for Gas and Dust

The Euler equations for perfectly coupled gas and dust in the three-dimensional Cartesian shearing box are

$$\begin{aligned} \frac{d\mathbf{v}}{dt} = & -2\Omega_{K0}\hat{\mathbf{z}} \times \mathbf{v} + (3\Omega_{K0}^2 x - 2\Omega_{K0}^2 r_0\eta_0)\hat{\mathbf{x}} - \Omega_{K0}^2 z\hat{\mathbf{z}} \\ & - \frac{1}{(\rho_g + \rho_d)} \nabla p_g, \end{aligned} \quad (8a)$$

$$\frac{d\rho_g}{dt} = -\rho_g \nabla \cdot \mathbf{v}, \quad (8b)$$

$$\frac{d\rho_d}{dt} = -\rho_d \nabla \cdot \mathbf{v}, \quad (8c)$$

$$\frac{ds_g}{dt} = 0, \quad s_g \equiv C_V \ln(p_g \rho_g^{-\gamma}) + s_{g0}, \quad (8d)$$

where \mathbf{v} is the velocity of a parcel of gas and dust, p_g , ρ_g , and s_g are the pressure, density, and entropy of the gas; ρ_d is the density of the dust; $\gamma \equiv C_P/C_V = 5/3$ is the ratio of specific heats at constant pressure and constant volume; the advective or Lagrangian derivative is defined $d/dt \equiv (\partial/\partial t + \mathbf{v} \cdot \nabla)$. The key difference between the dynamics of the gas and that of the dust is that we treat the dust as a cold, pressureless fluid.

The dust continuity equation can be recast in terms of the local dust-to-gas ratio: $d\mu/dt = 0$, that is, the local dust-to-gas ratio is an advectively conserved quantity, meaning that a parcel of fluid maintains its dust content. This is simply a consequence of the perfect coupling assumption which does not allow the dust component to slip apart from the gas component. This approximation is valid if the stopping time t_S (the e -folding time for a particle's velocity to match that of the surrounding medium because of frictional coupling) is much shorter than the timescales of interest for Kelvin–Helmholtz instability. For small particles for which the gas mean-free-path is larger than the size of the particles, Epstein drag sets this timescale (Cuzzi et al. 1993; Garaud et al. 2004)

$$\frac{t_{S,\text{epstein}}}{t_{\text{orb}}} \equiv \frac{\rho_s a / \rho_g c_s}{2\pi / \Omega_K} \sim 10^{-3} \left(\frac{a}{1 \text{ cm}} \right) \left(\frac{r}{1 \text{ AU}} \right)^{3/2}, \quad (9)$$

where ρ_s and a are the solid density and radius of a dust grain, and ρ_g and c_s are the gas density and sound speed.

Because we expect the Kelvin–Helmholtz instability to set in at low Mach number $\epsilon \sim \max(\delta, \lambda) \ll 1$, we invoke the anelastic approximation for the gas flow. We decompose the gas pressure and density into their dust-free equilibrium components (denoted by overbars) and fluctuating components (denoted by tildes) $p_g = \bar{p}_g + \tilde{p}_g$, $\rho_g = \bar{\rho}_g + \tilde{\rho}_g$. At low Mach number, the fluctuating components should scale as $\tilde{p}_g/\bar{p}_g \sim \tilde{\rho}_g/\bar{\rho}_g \sim \epsilon^2 \ll 1$. The gas pressure gradient and gas continuity equations can then be expanded

$$\frac{1}{\rho_g} \nabla p_g \approx \left[\frac{1}{\bar{\rho}_g} \nabla \bar{p}_g + \frac{1}{\bar{\rho}_g} \nabla \tilde{p}_g - \frac{\tilde{\rho}_g}{\bar{\rho}_g} \frac{1}{\bar{\rho}_g} \nabla \bar{p}_g \right] [1 + \mathcal{O}(\epsilon^4)], \quad (10a)$$

$$0 \approx [\nabla \cdot (\bar{\rho}_g \mathbf{v})] [1 + \mathcal{O}(\epsilon^2)]. \quad (10b)$$

The anelastic approximation has been extensively used in the study of deep, subsonic convection in planetary atmospheres (Ogura & Phillips 1962; Gough 1969) and stars (Gilman & Glatzmaier 1981; Glatzmaier & Gilman 1981a, 1981b). Barranco et al. (2000) and Barranco & Marcus (2000, 2005, 2006) previously used the anelastic approximation to study three-dimensional vortices in protoplanetary disks. One of the consequences of this approximation is that the total density is replaced by the time-independent mean density in the mass continuity equation, which has the effect of filtering high-frequency acoustic waves and shocks, but allowing slower wave phenomena such as internal gravity waves.

When the background temperature is spatially constant, we can eliminate from the equations of motion any explicit dependence on the mean density by using enthalpy $\tilde{h}_g \equiv \tilde{p}_g/\bar{\rho}_g$ instead of pressure, and temperature instead of entropy

$$\begin{aligned} -\frac{1}{\bar{\rho}_g} \nabla \tilde{p}_g + \frac{\tilde{\rho}_g}{\bar{\rho}_g} \frac{1}{\bar{\rho}_g} \nabla \tilde{p}_g &= -\nabla \tilde{h}_g - \frac{\tilde{T}}{T_0} \frac{1}{\bar{\rho}_g} \nabla \tilde{p}_g \\ &= -\nabla \tilde{h}_g + \frac{\tilde{T}}{T_0} (2\Omega_{K0}^2 r_0 \eta_0 \hat{\mathbf{x}} + \Omega_{K0}^2 z \hat{\mathbf{z}}). \end{aligned} \quad (11)$$

Note that terms with pressure fluctuations are absent from the right side of Equation (11) because their effect would be proportional to the gradient of the mean time-independent temperature, which is zero for uniform background temperature simulations.

Skipping a significant amount of algebra, the dynamic equations for coupled gas and dust with the constant temperature background and anelastic approximation become

$$\begin{aligned} \frac{d\mathbf{v}}{dt} &= -2\Omega_{K0} \hat{\mathbf{z}} \times \mathbf{v} + 3\Omega_{K0}^2 x \hat{\mathbf{x}} + \frac{\tilde{T}}{T_0} (2\Omega_{K0}^2 r_0 \eta_0 \hat{\mathbf{x}} + \Omega_{K0}^2 z \hat{\mathbf{z}}) \\ &\quad - \nabla \tilde{h}_g - \frac{\mu}{\mu+1} \left[\left(1 + \frac{\tilde{T}}{T_0} \right) (2\Omega_{K0}^2 r_0 \eta_0 \hat{\mathbf{x}} \right. \\ &\quad \left. + \Omega_{K0}^2 z \hat{\mathbf{z}}) - \nabla \tilde{h}_g \right], \end{aligned} \quad (12a)$$

$$0 = \nabla \cdot \bar{\rho}_g \mathbf{v}, \quad (12b)$$

$$\frac{d\mu}{dt} = 0, \quad \mu \equiv \rho_d/\bar{\rho}_g, \quad (12c)$$

$$C_P \frac{d\tilde{T}}{dt} = - \left(1 + \frac{\tilde{T}}{T_0} \right) \mathbf{v} \cdot (2\Omega_{K0}^2 r_0 \eta_0 \hat{\mathbf{x}} + \Omega_{K0}^2 z \hat{\mathbf{z}}), \quad (12d)$$

$$\tilde{p}_g = \bar{\rho}_g \mathcal{R} T_0 + \bar{\rho}_g \mathcal{R} \tilde{T}, \quad \tilde{h}_g \equiv \tilde{p}_g/\bar{\rho}_g. \quad (12e)$$

These equations are almost identical to the anelastic equations in Barranco & Marcus (2005, 2006), with the addition of a nonlinear forcing term for the inertia of the dust. Note that in going from the entropy Equation (8d) to the temperature Equation (12d), one must replace C_V with C_P in the final result. The reason is that although density fluctuations can be ignored in the continuity equation, they are not negligible in the energy/entropy equation. Including them leads to replacing C_V with C_P . This is a standard result for Boussinesq and anelastic approximations and is discussed by both Pedlosky (1979) and Kundu (1990).

The above set of dynamic equations allow the following steady-state equilibrium with dust (denoted by the dagger symbol):

$$0 = v_x^\dagger = v_z^\dagger = \tilde{T}^\dagger, \quad (13a)$$

$$\mu^\dagger(z) \text{ arbitrary}, \quad (13b)$$

$$v_y^\dagger(x, z) = -\frac{3}{2} \Omega_{K0} x + \left[\frac{\mu^\dagger(z)}{\mu^\dagger(z) + 1} \right] \Omega_{K0} r_0 \eta_0, \quad (13c)$$

$$\frac{d\tilde{h}_g^\dagger(z)}{dz} = -\mu^\dagger(z) \Omega_{K0}^2 z. \quad (13d)$$

In the limit where we take $\Lambda_g \rightarrow \infty$ and neglect the radial variation of the background gas density and radial component

of the gas buoyancy, one can derive the following global energy balance equations:

$$KE \equiv \int_V \frac{1}{2} (1 + \mu) \bar{\rho}_g \mathbf{v} \cdot \mathbf{v} dV, \quad (14a)$$

$$PE \equiv \int_V \left[\bar{\rho}_g \mu \Omega_{K0}^2 \left(2r_0 \eta_0 x + \frac{1}{2} z^2 - \frac{3}{2} x^2 \right) + C_P \bar{\rho}_g \tilde{T} \right] dV, \quad (14b)$$

$$\begin{aligned} \frac{d}{dt} (KE + PE) &= \frac{3}{2} \Omega_{K0} L_x \int_S [(1 + \mu) \bar{\rho}_g v_x \tilde{v}_y] |_{x=+L_x/2} dy dz \\ &\quad - 2\Omega_{K0}^2 r_0 \eta_0 L_x \int_S [\bar{\rho}_g \mu v_x] |_{x=+L_x/2} dy dz, \end{aligned} \quad (14c)$$

where $\tilde{v}_y \equiv v_y + \frac{3}{2} \Omega_{K0} x$ is the azimuthal velocity minus the background Keplerian shear flow.

2.3. Brief Description of Numerical Method

Here we briefly describe the numerical method; a more detailed presentation can be found in Barranco & Marcus (2006). We solve the dynamic Equations (12) with a spectral method; that is, each variable is represented as a finite sum of basis functions multiplied by spectral coefficients (Gottlieb & Orszag 1977; Marcus 1986; Canuto et al. 1988; Boyd 2000). The choice of basis functions for each direction is guided by the corresponding boundary conditions. The equations are autonomous in the azimuthal coordinate y , so it is reasonable to assume periodic boundary conditions in this direction. However, the equations explicitly depend on the radial coordinate x because of the linear background shear. We adopt ‘‘shearing box’’ boundary conditions: $q(x + L_x, y - (3/2)\Omega_0 L_x t, z, t) = q(x, y, z, t)$, where q represents any of \mathbf{v} , \tilde{h} , \tilde{T} , etc. In practice, we rewrite the Equations (12) in terms of quasi-Lagrangian or shearing coordinates that advect with the background shear (Goldreich & Lynden-Bell 1965; Marcus & Press 1977; Rogallo 1981): $t' \equiv t$, $x' \equiv x$, $y' \equiv y + (3/2)\Omega_0 x t$, and $z' \equiv z$. In these new coordinates, the radial boundary conditions become $q(x' + L_x, y', z', t') = q(x', y', z', t')$. That is, shearing box boundary conditions are equivalent to periodic boundary conditions in the shearing coordinates. Physically, this means that the periodic images at different radii are not fixed, but advect with the background shear.

In the shearing coordinates, the equations are autonomous in both x' and y' (although they now explicitly depend on t'), making a Fourier basis the natural choice for the spectral expansions in the horizontal directions:

$$q(x', y', z', t') = \sum_{\mathbf{k}} \hat{q}_{\mathbf{k}}(t') e^{ik'_x x'} e^{ik'_y y'} \phi_n(z'), \quad (15)$$

where q is any variable of interest, $\{\hat{q}_{\mathbf{k}}(t')\}$ is the set of spectral coefficients, and $\mathbf{k} = \{k'_x, k'_y, n\}$ is the set of wavenumbers. We have implemented the simulations with two different sets of basis functions for the spectral expansions in the vertical direction, corresponding to two different sets of boundary conditions:

1. For the truncated domain $-L_z \leq z \leq L_z$, we use Chebyshev polynomials $\phi_n(z) = T_n(z/L_z) \equiv \cos(n\xi)$, where $\xi \equiv \cos^{-1}(z/L_z)$. We apply the condition that the vertical velocity vanishes at the top and bottom boundaries $v_z(x, y, z = \pm L_z, t) = 0$.

2. For the infinite domain $-\infty < z < \infty$, we use rational Chebyshev functions $\phi_n(z) = \cos(n\xi)$ (for v_x , v_y , and all the thermodynamic variables) or $\phi_n(z) = \sin(n\xi)$ (for v_z), where $\xi \equiv \cot^{-1}(z/L_z)$. In this context, L_z is no longer the physical size of the box, but is a mapping parameter; exactly one half of the grid points are within $|z| \leq L_z$, whereas the other half are widely spaced in the region $L_z < |z| < \infty$. No explicit boundary conditions on the vertical velocity are necessary when we solve the equations on the infinite domain because the $\phi_n(z) = \sin(n\xi)$ basis functions individually decay to zero at large z .

The equations are integrated forward in time with a fractional step method: the nonlinear advection terms are integrated with an explicit second-order Adams–Bashforth method, and the pressure step is computed with a semi-implicit second-order Crank–Nicolson method. The time integration scheme is overall globally second-order accurate. Unlike finite-difference methods, spectral methods have no inherent grid dissipation; energy cascades to smaller and smaller size scales via the nonlinear interactions, where it can “pile-up” and potentially degrade the convergence of the spectral expansions. We employ a ∇^{12} hyperviscosity or low-pass filter every time step to damp the energy at the highest wavenumbers.

Different horizontal Fourier modes interact only through the nonlinear advective terms; once these terms are computed, the horizontal Fourier modes can be decoupled. This motivated us to parallelize the code: each processor computes on a different block of data in horizontal Fourier wavenumber space. Parallelization is implemented with Message Passing Interface (MPI), typically using between 64 and 512 processors. Wall-clock time scales inversely with the number of processors, indicating near-optimal parallelism; timing analyses are presented in Barranco & Marcus (2006).

3. REVISITING THE CASE OF NO DIFFERENTIAL ROTATION

The linear stability of settled dust layers to Kelvin–Helmholtz instability has previously been investigated by a number of researchers (Sekiya 1998; Sekiya & Ishitsu 2000; Youdin & Shu 2002; Garaud & Lin 2004; Gomez & Ostriker 2005); however, almost all of these analyses neglected the role of the differential rotation in the protoplanetary disk. If one were to directly linearize the Equations (12), one would find the resulting set to depend linearly on the radial coordinate x because of the shear, making it difficult to apply periodic boundary conditions in the radial direction. Alternatively, one could employ a set of coordinates that advect with the background shear (Goldreich & Lynden-Bell 1965; Marcus & Press 1977; Ryu & Goodman 1992), but then the resulting linearized equations would explicitly depend on time. Ishitsu & Sekiya (2003) employed this approach using an initial-value code to address the effect of horizontal shear on unstable eigenmodes in the small-amplitude, linear regime. They found that modes grew for a limited period of time, but were eventually stabilized as they were sheared out to high spatial wavenumber. No matter the approach, the linear stability analysis is difficult to treat analytically, motivating theorists to tackle the problem without the background shear with the hope that the results are qualitatively, if not quantitatively, useful in determining whether or not the Kelvin–Helmholtz instability is a barrier to further settling.

In this section, we briefly revisit the case of no radial shear, first without, and then with the Coriolis force. We

will neglect the x (radial) dependence of the background gas density (setting $\Lambda_g \rightarrow \infty$), which eliminates the radial component of gas buoyancy. We assume eigenmodes of the form $q'(t, x, y, z) = q'(z) \exp(-i\omega t + ik_x x + ik_y y)$. The linearized equations corresponding to Equation (12), *without* radial shear and radial gas buoyancy, are

$$-i\omega v'_x = -v'_y(z)ik_y v'_x + 2\Omega_{K0} v'_y - \left[\frac{ik_x}{[1 + \mu^\dagger(z)]} \right] h' - \left[\frac{2\Omega_{K0}^2 \eta_0 r_0}{[1 + \mu^\dagger(z)]^2} \right] \mu', \quad (16a)$$

$$-i\omega v'_y = -2\Omega_{K0} v'_x - v'_y(z)ik_y v'_y - \left[\frac{dv'_y}{dz} \right] v'_z - \left[\frac{ik_y}{[1 + \mu^\dagger(z)]} \right] h', \quad (16b)$$

$$-i\omega v'_z = -v'_y(z)ik_y v'_z - \left[\frac{(\partial/\partial z)}{[1 + \mu^\dagger(z)]} \right] h' + \left[\frac{\Omega_{K0}^2 z}{[1 + \mu^\dagger(z)]} \right] \frac{T'}{T_0} - \left[\frac{\Omega_{K0}^2 z}{[1 + \mu^\dagger(z)]} \right] \mu', \quad (16c)$$

$$-i\omega \frac{T'}{T_0} = -v'_y(z)ik_y \frac{T'}{T_0} + \left[\frac{\mathcal{R}}{C_P} \frac{d \ln \bar{\rho}_g}{dz} \right] v'_z, \quad (16d)$$

$$-i\omega \mu' = -v'_y(z)ik_y \mu' - \left[\frac{d\mu^\dagger}{dz} \right] v'_z, \quad (16e)$$

$$0 = ik_x v'_x + ik_y v'_y + \left[\frac{\partial}{\partial z} + \frac{d \ln \bar{\rho}_g}{dz} \right] v'_z. \quad (16f)$$

One can eliminate T' and μ' from the equation for v'_z , yielding

$$[-i\omega + v'_y(z)ik_y]^2 v'_z = - \left[\frac{-i\omega + v'_y(z)ik_y}{[1 + \mu^\dagger(z)]} \right] \frac{\partial h'}{\partial z} + \frac{\Omega_{K0}^2 z}{[1 + \mu^\dagger(z)]} \left(\frac{\mathcal{R}}{C_P} \frac{d \ln \bar{\rho}_g}{dz} + \frac{d\mu^\dagger}{dz} \right) v'_z. \quad (17)$$

This form allows us to easily identify the Brunt–Väisälä frequency

$$N^2 = - \frac{\Omega_{K0}^2 z}{[1 + \mu^\dagger(z)]} \left(\frac{\mathcal{R}}{C_P} \frac{d \ln \bar{\rho}_g}{dz} + \frac{d\mu^\dagger}{dz} \right). \quad (18)$$

Before proceeding with the linear analysis, we must specify the form of the vertical distribution of dust. We choose a Gaussian profile for the local dust-to-gas ratio:

$$\mu^\dagger(z) = \mu_0^\dagger \exp(-z^2/2H_\mu^2), \quad \mu_0^\dagger \equiv \frac{\Sigma_d H_g}{\Sigma_g H_d}, \\ H_\mu^{-2} \equiv H_d^{-2} - H_g^{-2}, \quad (19)$$

where we have defined the midplane dust-to-gas ratio μ_0^\dagger , the initial Gaussian scale height for the dust density H_d , and the initial Gaussian scale height for the dust-to-gas ratio H_μ .

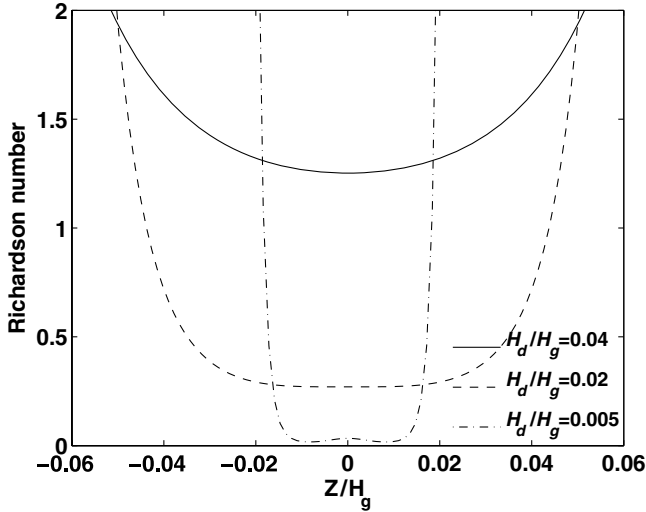


Figure 1. Gradient Richardson number (Equation (20)) for Gaussian profiles of the local dust-to-gas ratio μ . For these three curves, $\Sigma_d/\Sigma_g = 0.01$, $\eta_0 V_{K0}/c_{s0} = 0.1$, and $H_d/H_g = 0.04, 0.02, 0.005$, respectively corresponding to peak dust-to-gas ratios of $\mu_0^\dagger = 0.25, 0.50, 2.0$. For $\mu_0^\dagger = 1/2$, the Richardson number is at a minimum right at the midplane ($z = 0$) and is nearly constant throughout much of the dust layer before rising sharply at the edge of the dust distribution. For $\mu_0^\dagger > 1/2$, the Richardson number is still relatively constant throughout the core of the layer, although the minimum has shifted off the midplane.

The gradient Richardson number (Equation (1)) for a Gaussian distribution of dust is

$$Ri(z) = \left(\frac{\eta_0 V_{K0}}{c_{s0}} \right)^{-2} \left(\frac{H_\mu}{H_g} \right)^2 \frac{[1 + \mu^\dagger(z)]^3}{\mu^\dagger(z)} \times \left[1 + \frac{\mathcal{R}}{C_P} \frac{1}{\mu^\dagger(z)} \left(\frac{H_\mu}{H_g} \right)^2 \right]. \quad (20)$$

In Figure 1, we have graphed the gradient Richardson number with $\Sigma_d/\Sigma_g = 0.01$ and $\eta_0 V_{K0}/c_{s0} = 0.1$, for a few different dust scale heights. For $\mu_0^\dagger = 1/2$ ($H_d/H_g = 0.02$), the Richardson number is at a minimum right at the midplane ($z = 0$) and is nearly constant throughout much of the dust layer before rising sharply at the edge of the dust distribution. For $\mu_0^\dagger > 1/2$ ($H_d/H_g < 0.02$), the Richardson number is still relatively constant throughout the core of the layer, although the minimum has shifted off the midplane. For very thin dust layers, we can ignore the gas buoyancy near the midplane (i.e., the \mathcal{R}/C_P term on the far right of Equation (20)); the minimum gradient Richardson number is thus

$$Ri_{\min} = \left(\frac{\eta_0 V_{K0}}{c_{s0}} \right)^{-2} \left(\frac{H_\mu}{H_g} \right)^2 \times \begin{cases} (27/4) & \text{at } z = \pm H_\mu \sqrt{2 \ln(2\mu_0^\dagger)} \text{ for } \mu_0^\dagger > 1/2 \\ (1 + \mu_0^\dagger)^3 / \mu_0^\dagger & \text{at } z = 0 \text{ for } \mu_0^\dagger < 1/2. \end{cases} \quad (21)$$

It is interesting to note that for dust-rich layers ($\mu_0^\dagger > 1/2$), the minimum Richardson number is independent of the dust-to-gas ratio.

We numerically solve the eigenproblem (Equation (16)) for the complex frequencies ω with a Chebyshev spectral method in which the top and bottom boundaries are mapped to infinity

(Barranco & Marcus 2006; Boyd 2000; Cain et al. 1984). Because we are neglecting differential rotation, we invoke Squire’s theorem which states that two-dimensional eigenmodes are more unstable than three-dimensional ones (Squire 1933; Chandrasekhar 1961; Drazin & Reid 1981), and so set $k_x = 0$. We also restrict our analysis to modes for which the dust-to-gas ratio perturbation μ' is an odd-function of the vertical coordinate z . These modes were found to be more unstable by Garaud & Lin (2004) and Gomez & Ostriker (2005).

3.1. Case of no Coriolis Force and no Horizontal Shear

Figure 2 shows the growth rates (imaginary part of the complex eigenvalue ω) for the case where the Coriolis force is turned-off. Each of the twenty plots corresponds to different values of the global dust-to-gas ratio, Σ_d/Σ_g , and the strength of the radial gas pressure gradient, $\eta_0 V_{K0}/c_{s0}$, which sets the maximum differential velocity between pure dust and pure gas. The global dust-to-gas ratio varies across rows with values $\Sigma_d/\Sigma_g = 0.08, 0.04, 0.02, 0.01, 0.005$. The strength of the radial pressure gradient varies down columns with values $\eta_0 V_{K0}/c_{s0} = 0.2, 0.1, 0.05, 0.025$. The horizontal axis of each individual plot is the nondimensionalized wavenumber $(8/\pi)H_d k_y$, and the vertical axis is the ratio of the dust scale height to the gas scale height. The solid contours, from outer to inner, correspond to growth rates of 0.1, 0.2, 0.3, 0.4, 0.5, 0.6 in units of Ω_{K0}^{-1} . The outermost (dotted) contour corresponds to an extrapolation to zero growth rate.

The peak of the zero growth contour reveals the thinnest layer to remain stable to Kelvin–Helmholtz instability as well as the wavelength of the eigenmode at the onset of instability. The wavelength at onset is typically between 8 and 16 times the dust scale height over the range of parameter space explored. In Figure 3, we plot contours in the $(\Sigma_d/\Sigma_g, \eta_0 V_{K0}/c_{s0})$ plane for the minimum dust scale height H_d/H_g (solid black lines) to remain stable. We also plot contours (dotted lines) for the minimum gradient Richardson number (Equation (21)) corresponding to the minimum dust thickness at the onset of instability. Over the range of parameter space explored, the minimum Richardson number is in the range 0.18 to 0.25, as expected for “classic” Kelvin–Helmholtz instability with no Coriolis force and no horizontal shear. Very similar results were obtained by Garaud & Lin (2004; especially compare with Figure 11 in their work), who investigated the stability of slowly settling dust layers with a two-fluid formulation.

We simulate the nonlinear evolution of the instability in order to investigate the nature of the subsequent mixing of gas and dust. An example of a two-dimensional simulation in the y – z plane with $\Sigma_d/\Sigma_g = 0.01$ and $\eta_0 V_{K0}/c_{s0} = 0.1$ is presented in Figure 4. The initial dust scale height is $H_d/H_g = 0.01$, corresponding to a peak local dust-to-gas ratio in the midplane of $\mu_0^\dagger = 1$ and a minimum Richardson number of $Ri_{\min} = 0.0675$. Dust layers in equilibrium were initialized according to Equations (13) and (19), and then perturbations were added to the dust-to-gas ratio μ

$$\mu(y, z) = \mu^\dagger(z) \left\{ 1 + A(y) [\cos(\pi z/2H_\mu) + \sin(\pi z/2H_\mu)] \right\}. \quad (22)$$

The amplitude function $A(y)$ is constructed in wavenumber space so that each Fourier mode has random phase and an amplitude inversely proportional to horizontal wavenumber $\hat{A}(k_y) \propto k_y^{-1}$. The linear stability analysis above predicts that the most unstable eigenmode has a wavelength of $\lambda_c = 10.7H_d$ and an e -folding time of $t_e = 0.32t_{\text{orb}}$. The first column illustrates

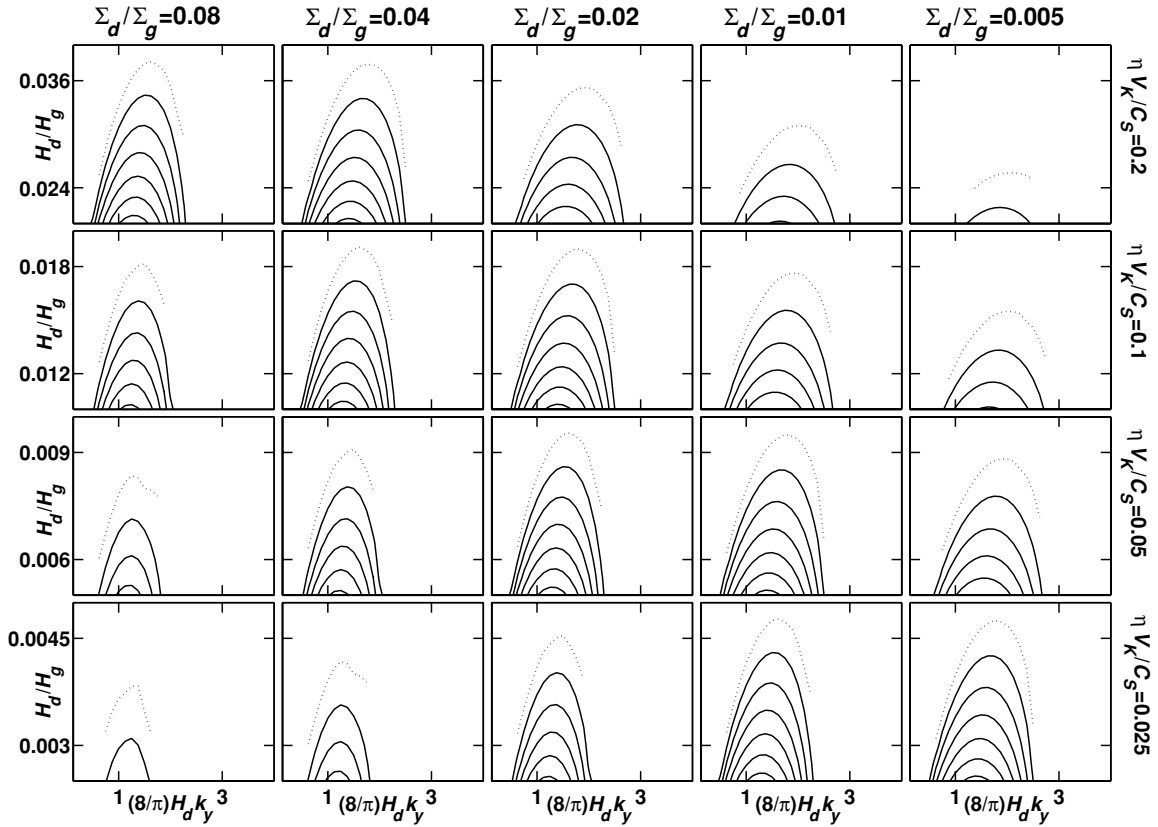


Figure 2. Contour plots of growth rates of Kelvin–Helmholtz instability for the case of no Coriolis force and no horizontal shear. The global dust-to-gas ratio varies across rows with values $\Sigma_d/\Sigma_g = 0.08, 0.04, 0.02, 0.01, 0.005$. The strength of the radial pressure gradient varies down columns with values $\eta_0 V_{K0}/c_{s0} = 0.2, 0.1, 0.05, 0.025$. The horizontal axis of each plot is the nondimensionalized wavenumber $(8/\pi)H_d k_y$, and the vertical axis is the ratio of the dust scale height to the gas scale height. The solid contours, from outer to inner, correspond to growth rates of 0.1, 0.2, 0.3, 0.4, 0.5, 0.6 in units of Ω_{K0}^{-1} . The outermost, dotted contour corresponds to an extrapolation to zero growth rate.

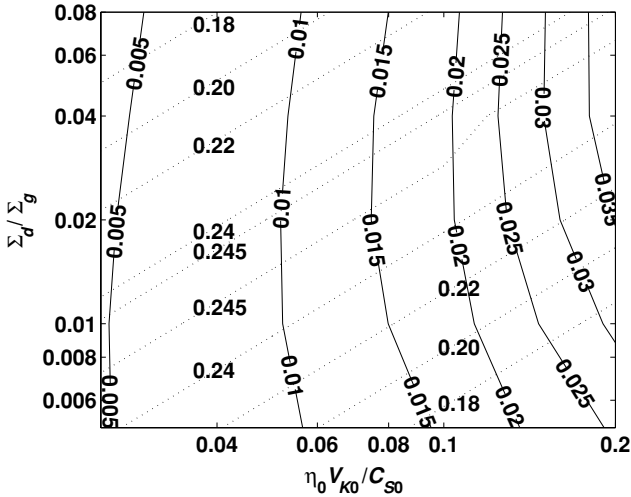


Figure 3. Contours in the $(\Sigma_d/\Sigma_g, \eta_0 V_{K0}/c_{s0})$ plane for the minimum dust layer thickness H_d/H_g (solid black lines) and minimum Richardson number $R_{i,min}$ (dotted lines) at the onset of instability. Over the range of parameter space explored, the minimum Richardson number is in the range 0.18–0.25, as expected for “classic” Kelvin–Helmholtz instability with no Coriolis force and no horizontal shear. Note how the contours for H_d/H_g are nearly vertical, indicating a weak dependence on the global dust-to-gas ratio for the onset of instability. This figure is consistent with Figure 11 in Garaud & Lin (2004).

the evolution of the local dust-to-gas ratio μ (deep red = 1, deep blue = 0); the second column shows the evolution of the radial component of vorticity $\omega_x \equiv \partial v_z/\partial y - \partial v_y/\partial z$ (red = vorticity that points into the page, blue = vorticity that points

out of the page). The times corresponding to each frame, in units of the orbital period, are 3.8, 4.5, 5.1, 5.7, 15.3. The dust layer develops waves, which grow and break into pairs of anti-aligned vortices. Note the excellent agreement between the observed wavelength and that theoretically predicted by the linear stability analysis. Characteristic of two-dimensional turbulence, like-signed vortices merge to form larger vortices as energy cascades to larger spatial scales. These vortices chaotically interact, leading to thorough mixing of the dust with the gas. After the dust and gas are thoroughly mixed, resettling is not allowed because of the perfect coupling assumption. The turbulence slowly decays away because the only driver is the Kelvin–Helmholtz instability.

3.2. Case with Coriolis Force, but no Horizontal Shear

Figure 5 shows the growth rates for the case with the Coriolis force, but no horizontal shear. As before, each of the twenty plots corresponds to different values of the global dust-to-gas ratio, Σ_d/Σ_g , and the strength of the radial gas pressure gradient, $\eta_0 V_{K0}/c_{s0}$, which sets the maximum differential velocity between pure dust and pure gas. The global dust-to-gas ratio varies across rows with values $\Sigma_d/\Sigma_g = 0.08, 0.04, 0.02, 0.01, 0.005$. The strength of the radial pressure gradient varies down columns with values $\eta_0 V_{K0}/c_{s0} = 0.2, 0.1, 0.05, 0.025$. The horizontal axis of each individual plot is the nondimensionalized wavenumber $(8/\pi)H_d k_y$, and the vertical axis is the ratio of the dust scale height to the gas scale height. The solid contours, from outer to inner, correspond to growth rates of 0.1, 0.2,

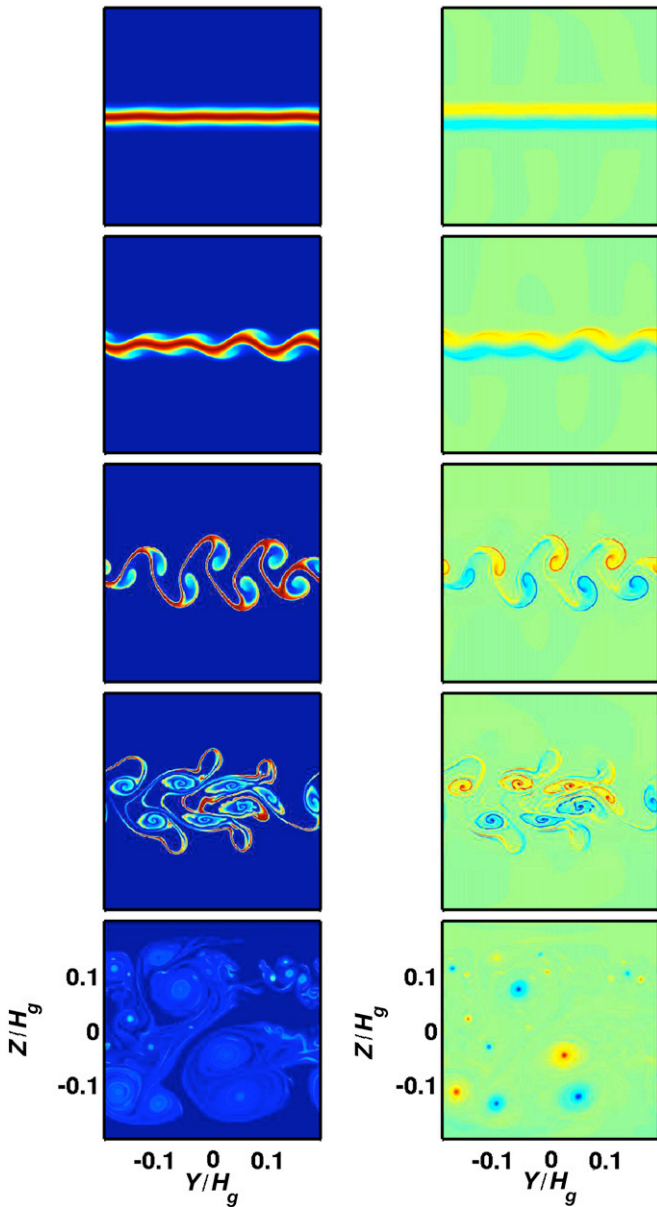


Figure 4. Two-dimensional nonlinear evolution of Kelvin–Helmholtz instability with no Coriolis force and no horizontal shear. In this simulation, $\Sigma_d/\Sigma_g = 0.01$ and $\eta_0 V_{K0}/c_{s0} = 0.1$. The initial dust scale height is $H_d/H_g = 0.01$, corresponding to a peak local dust-to-gas ratio in the midplane of $\mu_0^\dagger = 1$ and a minimum Richardson number of $Ri_{\min} = 0.0675$. The first column illustrates the evolution of the local dust-to-gas ratio μ (deep red = 1, deep blue = 0); the second column shows the evolution of the radial component of vorticity ω_x (red = vorticity that points into the page, blue = vorticity that points out of the page). The times corresponding to each frame, in units of the orbital period, are 3.8, 4.5, 5.1, 5.7, 15.3.

(A color version of this figure is available in the online journal.)

0.3, 0.4, 0.5, 0.6 in units of Ω_{K0}^{-1} . Note that the vertical scale of each plot is a factor of 2.2 larger than the corresponding ones in Figure 2, and the horizontal scale is a factor of 2 larger.

Gomez & Ostriker (2005) were the first to note that settled dust layers are more unstable when the Coriolis force is included. Instability occurs for thicker layers and for a much larger range of wavenumbers. In the case where there is no Coriolis force, the range of unstable wavenumbers for a given ratio of H_d/H_g is relatively narrow. In contrast, when the Coriolis force is included, we find that instability occurs for very large

wavenumbers, with no apparent upper limit. However, these large wavenumber (small wavelength) eigenmodes are the ones which will be most affected by the inclusion of horizontal shear. Note that the contours in Figure 5 get increasingly jagged as the growth rate gets closer to zero. This is purely a limitation of the numerical algorithm and is not physical. Our algorithm has difficulty simultaneously resolving both the thickness of the dust layer and the very small wavelength features associated with the instability. Increased resolution certainly helps, but becomes prohibitively expensive time wise if one seeks to explore wide range of parameter space.

Figure 6 shows the two-dimensional nonlinear evolution of Kelvin–Helmholtz instability with Coriolis force but still no horizontal shear. This simulation is exactly the same as the one in Figure 4, except that the Coriolis force is included. As before $\Sigma_d/\Sigma_g = 0.01$, $\eta_0 V_{K0}/c_{s0} = 0.1$, $H_d/H_g = 0.01$, $\mu_0^\dagger = 1$, and $Ri_{\min} = 0.0675$. Perturbations were added to the local dust-to-gas ratio with the same prescription as in the previous section. The linear stability analysis above predicts that the most unstable eigenmode has a wavelength of $\lambda_c = 8.0H_d$ and an e -folding time of $t_e = 0.28t_{\text{orb}}$. The first column illustrates the evolution of the local dust-to-gas ratio μ (deep red = 1, deep blue = 0); the second column shows the evolution of the radial component of vorticity ω_x (red = vorticity that points into the page, blue = vorticity that points out of the page). The times corresponding to each frame, in units of the orbital period, are 1.9, 2.2, 2.5, 2.9, 7.6. Waves appear on the dust layer as with the case with no Coriolis force, but no large-scale vortices develop. Again, the agreement between the observed wavelength and the theoretically predicted one is excellent. The vorticity has more power at the smallest spatial scales. The nonlinear mixing, however, is still very efficient, and the dust is completely remixed with the gas throughout the entire computational domain. As before, the dust cannot resettle because of the perfect-coupling assumption. The turbulence decays away, leaving a laminar, well-mixed flow.

We also simulate a thick dust layer that would have been unambiguously stable if there was no Coriolis force. Figure 7 shows the two-dimensional nonlinear evolution for the case $\Sigma_d/\Sigma_g = 0.01$, $\eta_0 V_{K0}/c_{s0} = 0.1$, $H_d/H_g = 0.04$, $\mu_0^\dagger = 0.25$, and $Ri_{\min} = 1.25$. The linear stability analysis above predicts that the most unstable eigenmode has a wavelength of $\lambda_c = 3.2H_d$ and an e -folding time of $t_e = 1.8t_{\text{orb}}$. The times corresponding to each frame, in units of the orbital period, are 3.2, 3.8, 4.5, 5.1, 7.6. The instability sets in at a very small wavelength, fully consistent with the value determined in the linear stability analysis in Figure 5. The fact that the Coriolis force appears to be destabilizing was first recognized by Gomez & Ostriker (2005), who found that the dust layers were unstable for Richardson numbers up to approximately 5, in contrast to the classical Kelvin–Helmholtz instability with a critical Richardson number of around 0.25 (especially see their Figure 9). In the next section, we explore the effect of horizontal shear on the evolution of the instability of such thick layers.

4. THREE-DIMENSIONAL SIMULATIONS WITH RADIAL SHEAR

We present a series of fully three-dimensional simulations of settled dust layers with the Coriolis force and differential rotation; Table 1 contains a listing of parameters for these simulations. Dust layers in equilibrium were initialized according to Equations (13) and (19), and then perturbations were

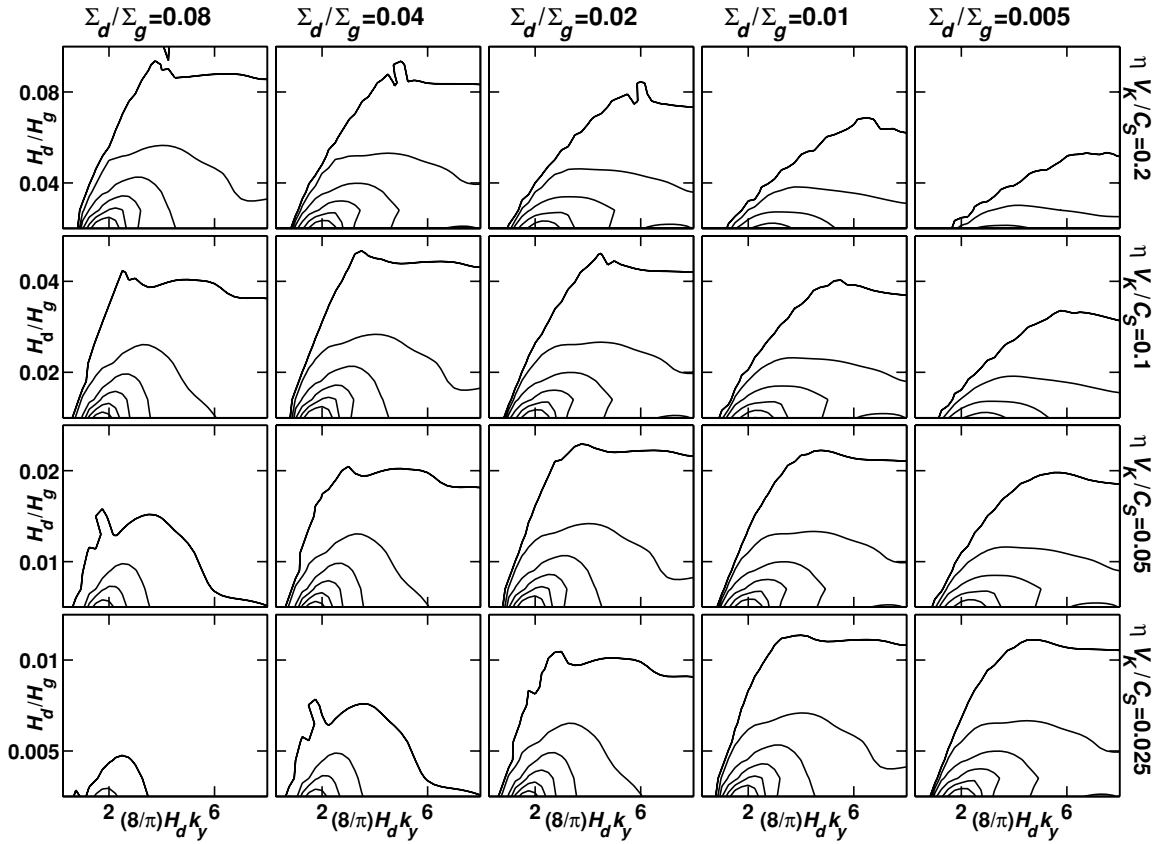


Figure 5. Contour plots of growth rates of Kelvin–Helmholtz instability for the case with the Coriolis force, but no horizontal shear. The global dust-to-gas ratio varies across rows with values $\Sigma_d/\Sigma_g = 0.08, 0.04, 0.02, 0.01, 0.005$. The strength of the radial pressure gradient varies down columns with values $\eta_0 V_{K0}/c_{s0} = 0.2, 0.1, 0.05, 0.025$. The horizontal axis of each plot is the nondimensionalized wavenumber $(8/\pi)H_d k_y$, and the vertical axis is the ratio of the dust scale height to the gas scale height. The solid contours, from outer to inner, correspond to growth rates of 0.1, 0.2, 0.3, 0.4, 0.5, 0.6 in units of Ω_{K0}^{-1} . Note that the horizontal and vertical axes of each plot have roughly twice the range as the corresponding plots in Figure 2 for the case of no Coriolis force.

Table 1
3D simulations of settled dust layers.

Run	(L_x, L_y, L_z)	(N_x, N_y, N_z)	$\eta_0 V_{K0}/c_{s0}$	Σ_d/Σ_g	H_d/H_g	Initial μ_{\max}	Initial Ri_{\min}	A_{rms}	Final Ri_{\min}	Final μ_{\max}
1	(0.1, 0.4, 0.4)	(32, 128, 256)	0.1	0.01	0.01	1.00	0.0675	0.01	0.42	0.41
2	(0.1, 0.4, 0.4)	(32, 128, 256)	0.1	0.01	0.01	1.00	0.0675	0.004	Stable	
3	(0.1, 0.4, 0.4)	(32, 128, 256)	0.1	0.01	0.01	1.00	0.0675	0.001	Stable	
4	(0.1, 0.4, 0.4)	(32, 128, 256)	0.1	0.01	0.02	0.50	0.270	0.1	Stable	
5	(0.1, 0.4, 0.4)	(32, 128, 256)	0.1	0.01	0.02	0.50	0.270	0.2	Stable	
6	(0.1, 0.4, 0.4)	(32, 128, 256)	0.1	0.01	0.015	0.67	0.152	0.1	0.23	0.52
7	(0.1, 0.4, 0.4)	(32, 128, 256)	0.1	0.01	0.015	0.67	0.152	0.04	Stable	
8	(0.05, 0.2, 0.2)	(32, 128, 256)	0.1	0.01	0.005	2.00	0.0169	10^{-6}	0.28	0.49
9	(0.1, 0.4, 0.4)	(32, 128, 256)	0.1	0.01	0.005	2.00	0.0169	10^{-6}	0.38	0.43
10	(0.1, 0.4, 0.4)	(32, 128, 256)	0.1	0.02	0.01	2.00	0.0675	0.1	0.36	0.83
11	(0.1, 0.4, 0.4)	(32, 128, 256)	0.1	0.04	0.01	4.00	0.0675	0.1	0.43	1.70
12	(0.1, 0.4, 0.4)	(32, 128, 256)	0.1	0.08	0.01	8.00	0.0675	0.1	0.47	4.13
13	(0.1, 0.4, 0.4)	(32, 128, 256)	0.1	0.02	0.02	1.00	0.270	0.1	Stable	
14	(0.1, 0.4, 0.4)	(32, 128, 256)	0.1	0.04	0.02	2.00	0.270	0.1	Stable	
15	(0.1, 0.4, 0.4)	(32, 128, 256)	0.1	0.08	0.02	4.00	0.270	0.1	Stable	
16	(0.05, 0.2, 0.2)	(32, 128, 256)	0.1	0.02	0.005	4.00	0.0169	0.001	0.28	0.85
17	(0.05, 0.2, 0.2)	(32, 128, 256)	0.1	0.04	0.005	8.00	0.0169	0.001	0.30	1.71
18	(0.05, 0.2, 0.2)	(32, 128, 256)	0.1	0.08	0.005	16.0	0.0169	0.001	0.40	4.14
19	(0.1, 0.4, 0.4)	(32, 128, 256)	0.2	0.01	0.02	0.50	0.0675	0.01	0.21	0.30
20	(0.1, 0.4, 0.4)	(32, 128, 256)	0.2	0.01	0.04	0.25	0.313	0.1	Stable	
21	(0.1, 0.4, 0.4)	(32, 128, 256)	0.2	0.01	0.01	1.00	0.0169	0.01	0.22	0.29
22	(0.05, 0.2, 0.2)	(32, 128, 256)	0.05	0.01	0.01	1.00	0.270	0.04	Stable	
23	(0.05, 0.2, 0.2)	(32, 128, 256)	0.05	0.01	0.005	2.00	0.0675	0.04	0.32	0.83
24	(0.05, 0.2, 0.2)	(32, 128, 256)	0.05	0.01	0.0025	4.00	0.0169	0.04	0.32	0.79
25	(0.1, 0.4, 0.4)	(64, 256, 512)	0.1	0.01	0.01	1.00	0.0675	0.01	0.22	0.52
26	(0.1, 0.4, 0.4)	(64, 256, 512)	0.1	0.01	0.01	1.00	0.0675	0.001	Stable	
27	(0.05, 0.2, 0.2)	(64, 256, 512)	0.1	0.01	0.005	2.00	0.0169	10^{-6}	0.21	0.49

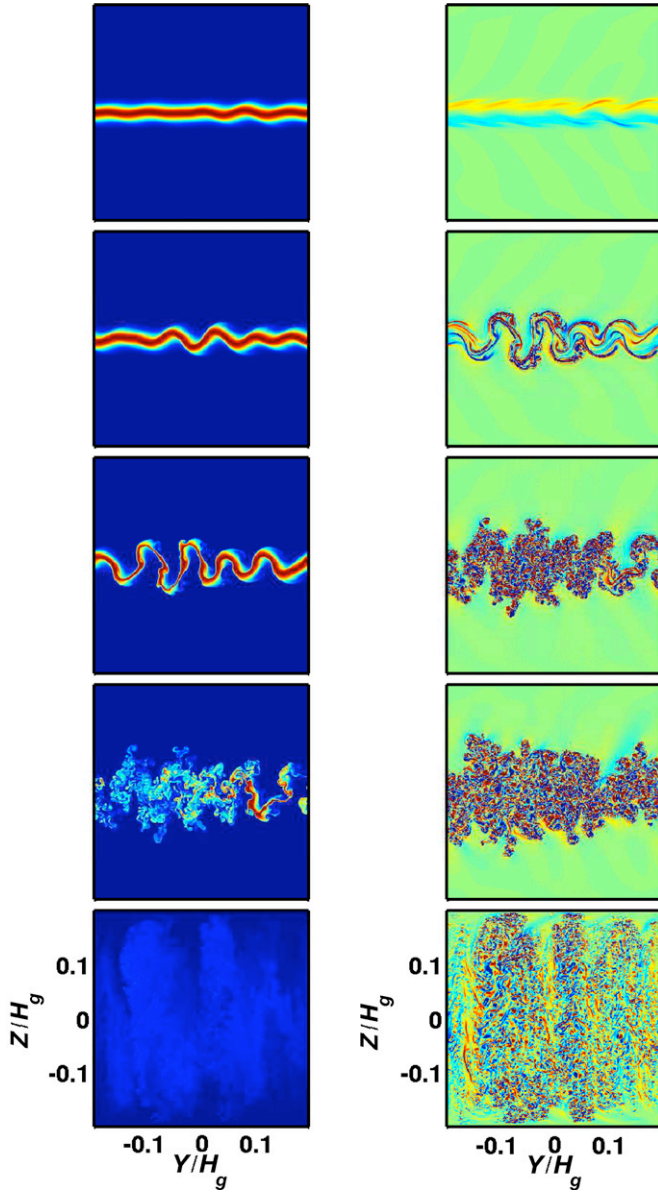


Figure 6. Two-dimensional nonlinear evolution of Kelvin–Helmholtz instability with Coriolis force but still no horizontal shear. In this simulation, $\Sigma_d/\Sigma_g = 0.01$ and $\eta_0 V_{K0}/c_{s0} = 0.1$. The initial dust scale height is $H_d/H_g = 0.01$, corresponding to a peak local dust-to-gas ratio in the midplane of $\mu_0^\dagger = 1$ and a minimum Richardson number of $Ri_{\min} = 0.0675$. The first column illustrates the evolution of the local dust-to-gas ratio μ (deep red = 1, deep blue = 0); the second column shows the evolution of the radial component of vorticity ω_x (red = vorticity that points into the page, blue = vorticity that points out of the page). The times corresponding to each frame, in units of the orbital period, are 1.9, 2.2, 2.5, 2.9, 7.6.

(A color version of this figure is available in the online journal.)

added to the dust-to-gas ratio μ

$$\mu(x, y, z) = \mu^\dagger(z) \{1 + A(x, y) [\cos(\pi z/2H_\mu) + \sin(\pi z/2H_\mu)]\}. \quad (23)$$

The amplitude function $A(x, y)$ is constructed in wavenumber space so that each Fourier mode has random phase and an amplitude inversely proportional to horizontal wavenumber $\hat{A}(k_\perp) \propto k_\perp^{-1}$. The perturbations were also forced to be antisymmetric about the x axis so that the initial kinetic and potential energies (Equations (14)) were unchanged. Thus, any observed mixing is due to instability and not due to the fact that

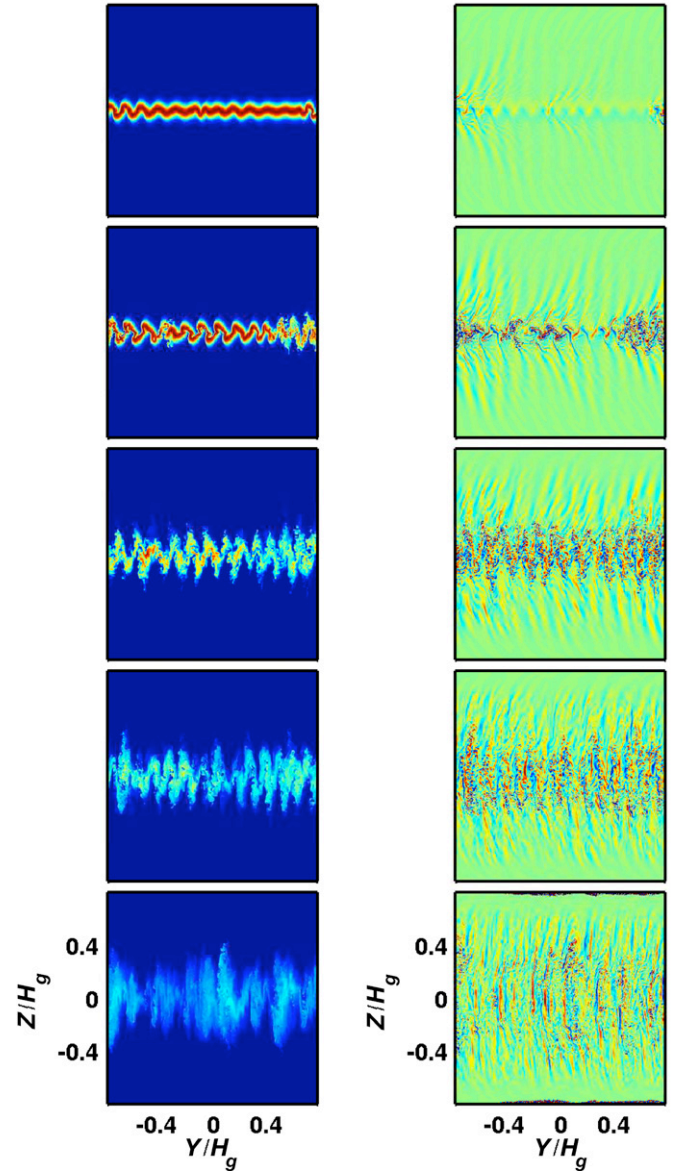


Figure 7. Two-dimensional nonlinear evolution of Kelvin–Helmholtz instability with Coriolis force but still no horizontal shear. In this simulation, $\Sigma_d/\Sigma_g = 0.01$ and $\eta_0 V_{K0}/c_{s0} = 0.1$. The initial dust scale height is $H_d/H_g = 0.04$, corresponding to a peak local dust-to-gas ratio in the midplane of $\mu_0^\dagger = 0.25$ and a minimum Richardson number of $Ri_{\min} = 1.25$. The first column illustrates the evolution of the local dust-to-gas ratio μ (deep red = 0.25, deep blue = 0); the second column shows the evolution of the radial component of vorticity ω_x (red = vorticity that points into the page, blue = vorticity that points out of the page). The times corresponding to each frame, in units of the orbital period, are 3.2, 3.8, 4.5, 5.1, 7.6.

(A color version of this figure is available in the online journal.)

energy was injected into the system. In Table 1, the amplitude A_{rms} is the rms of these dust-to-gas ratio perturbations in the midplane $z = 0$. Although the form of these perturbations may appear overly restrictive, what matters is that all the relevant eigenmodes of the linear problem have some initial power.

4.1. The Dependence on Initial Amplitude of Perturbations

Figures 8 and 9 show the results of Run 25, with $\Sigma_d/\Sigma_g = 0.01$, $\eta_0 V_{K0}/c_{s0} = 0.1$, $H_d/H_g = 0.01$, $\mu_0^\dagger = 1$, and initial $Ri_{\min} = 0.0675$. These are the same parameters as those used in the two-dimensional runs with no horizontal shear shown

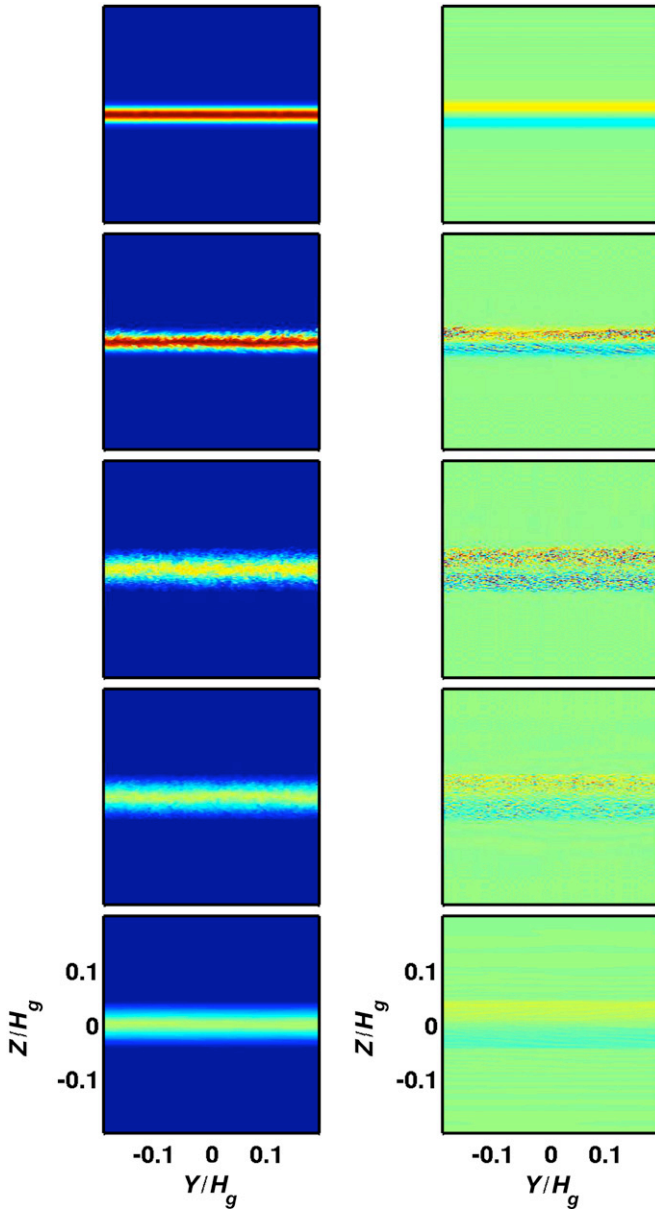


Figure 8. Three-dimensional nonlinear evolution of Kelvin–Helmholtz instability with Coriolis force and horizontal shear for Run 25. In this simulation, $\Sigma_d/\Sigma_g = 0.01$, and $\eta_0 V_{K0}/c_{s0} = 0.1$. The initial dust scale height is $H_d/H_g = 0.01$, corresponding to a peak local dust-to-gas ratio in the mid-plane of $\mu_0^\dagger = 1.0$ and a minimum Richardson number of $Ri_{\min} = 0.0675$. The amplitude of initial perturbations was $A_{\text{rms}} = 10^{-2}$. The panels show two-dimensional y – z ($\phi - z$) slices at $x = 0$ ($r = r_0$). The first column illustrates the evolution of the local dust-to-gas ratio μ (deep red = 1.0, deep blue = 0); the second column shows the evolution of the radial component of vorticity ω_x (red = vorticity that points into the page, blue = vorticity that points out of the page). The time interval between frames is 3.4 orbital periods.

(A color version of this figure is available in the online journal.)

in Figure 4 (no Coriolis force) and Figure 6 (with Coriolis force). The perturbations in Run 25 had initial amplitude $A_{\text{rms}} = 0.01$ (see also Run 1 at a lower resolution). Run 26 had exactly the same parameters as Run 25, except the amplitude of perturbations was reduced by a factor of 10 (see also Runs 2 and 3). This layer is unstable according to the classical Richardson criterion, as demonstrated in the previous section for the cases without horizontal shear. However, with the addition of horizontal shear, the stability of the dust layer depends also on the amplitude of the initial perturbations: if the magnitude of

perturbations is below some threshold, the layer remains stable; whereas if the amplitude exceeds some critical amount, the layer suffers Kelvin–Helmholtz instability. As found by Ishitsu & Sekiya (2003), unstable eigenmodes have a finite period of growth before the shear stretches them out to high wavenumber and damps further growth. The nonlinear evolution of a dust layer depends on whether the unstable eigenmodes were able to reach a sufficient amplitude to trigger nonlinear interactions, resulting eventually in turbulence and mixing of the dust with the gas. We have found through experimentation that the exact critical amplitude depends on such factors as the kind and shape of perturbations (e.g., perturbations to the dust-to-gas ratio, or temperature, or velocity field), the resolution (number of spectral modes), and the kind and magnitude of small-scale dissipation (i.e., hyperviscosity) in the code.

In Runs 6 and 7, we make the dust layer 50% thicker than the layer in Run 25: $\Sigma_d/\Sigma_g = 0.01$, $\eta_0 V_{K0}/c_{s0} = 0.1$, $H_d/H_g = 0.015$, $\mu_0^\dagger = 0.667$, and initial $Ri_{\min} = 0.152$. The amplitudes of initial perturbations were $A_{\text{rms}} = 0.1$ and $A_{\text{rms}} = 0.04$, respectively. A layer of this thickness would be unstable according to the Richardson criterion. We again find that the stability depends on the amplitude of perturbations. Because this layer is closer to stability than the one in Run 25, the eigenmodes would have a slower rate of growth; we would expect that such modes would have to start out at a larger amplitude in order for them to grow to sufficient amplitude to trigger nonlinear effects before the shear damped further growth. This is indeed the case as the critical amplitude is roughly an order of magnitude higher than the one for the layer half as thick.

Runs 4 and 5 are for layers that are twice as thick as in Run 25: $\Sigma_d/\Sigma_g = 0.01$, $\eta_0 V_{K0}/c_{s0} = 0.1$, $H_d/H_g = 0.02$, $\mu_0^\dagger = 0.5$, and $Ri_{\min} = 0.270$. The amplitudes of initial perturbations were $A_{\text{rms}} = 0.1$ and $A_{\text{rms}} = 0.2$, respectively. These layers are close to the critical Richardson number for stability in the absence of Coriolis force or shear, but would be unstable with the Coriolis force and no horizontal shear. In three-dimensional simulations with horizontal shear, these layers are found to be stable to even relatively large amplitude perturbations. Thus, it appears that the high-Richardson-number unstable flows with the Coriolis force first investigated by Gomez & Ostriker (2005) are stabilized by the horizontal shear.

For thinner layers than those in Run 25, however, the amplitude threshold practically vanishes. Runs 8, 9, and 27 are for a layer initially half as thick (Richardson number four times smaller): $\Sigma_d/\Sigma_g = 0.01$, $\eta_0 V_{K0}/c_{s0} = 0.1$, $H_d/H_g = 0.005$, $\mu_0^\dagger = 2.0$, and $Ri_{\min} = 0.0169$. The amplitude of perturbations was only 10^{-6} in these runs, yet the layers were still unstable. Figures 10 and 11 show the time evolution of this layer. There may indeed be a threshold, but it would be so low as to be practically irrelevant to the evolution of dust layers in real protoplanetary disk environments.

4.2. Nonlinear Mixing and Final States

In simulations without horizontal shear, the turbulence filled the computational domain and almost completely mixed the dust with the gas. There was little evidence of a remaining dust layer and the dust-to-gas ratio was nearly uniform. However, in three-dimensional simulations with horizontal shear, the turbulence and mixing were locally confined to a region above and below the original layer, resulting in the formation of a new, thicker layer. Figure 12(a) shows the horizontally-averaged dust-to-gas ratio as a function of height for the initial and final dust

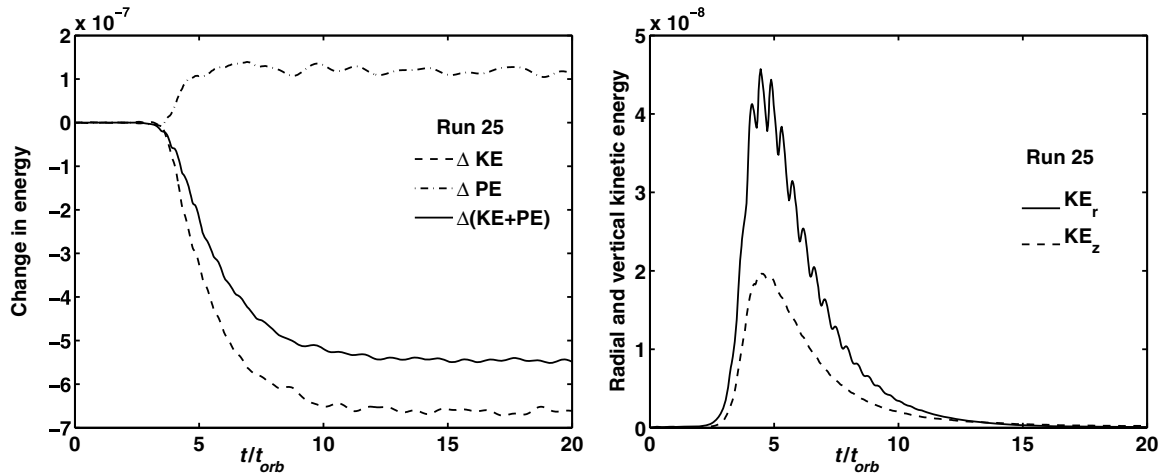


Figure 9. Evolution of energy for Run 25. In this simulation, $\Sigma_d/\Sigma_g = 0.01$ and $\eta_0 V_{K0}/c_{s0} = 0.1$. The initial dust scale height is $H_d/H_g = 0.01$, corresponding to a peak local dust-to-gas ratio in the midplane of $\mu_0^\dagger = 1.0$ and a minimum Richardson number of $Ri_{\min} = 0.0675$. The amplitude of initial perturbations was $A_{\text{rms}} = 10^{-2}$. The first column illustrates the evolution of the kinetic, potential, and total energies as functions of time; the second column shows the evolution of the radial and vertical components of the kinetic energy. There is a burst of turbulence associated with the nonlinear evolution of the Kelvin–Helmholtz instability: kinetic energy of the vertical shear is converted into gravitational potential energy as the heavier dust is lifted out of the gravitational potential well and mixed with the gas. However, once the layer reaches a new, thicker equilibrium, the turbulence decays away and the flow again becomes laminar.

layers in Runs 1, 8, 9, 25, and 27. Runs 1 and 25 had the same parameters, except Run 25 (approximately 26 collocation points across the dust layer) had twice the resolution as Run 1 (approximately 13 collocation points across the dust layer). The final equilibrium dust layer in Run 1 was approximately 27% thicker than the final layer in Run 25. The minimum Richardson number scales roughly with the square of the dust layer thickness (see Equation (21)), so this almost entirely explains the difference in the final minimum Richardson number for these two simulations. Runs 9, 8, and 27 had similar parameters, except Run 27 (approximately 26 collocation points across the dust layer) had twice the resolution as Run 8 (approximately 13 collocation points), which in turn had twice the resolution as Run 9 (approximately 6 collocation points). The final dust layer thickness for the low resolution Run 9 was approximately 14% thicker than that in Runs 8 and 27, which had nearly identical final layer thicknesses. The trend is that the lower resolution runs tend to have slightly thicker final layers. We suggest that the lower resolution runs had coarser turbulence which resulted in enhanced mixing.

Figures 9 and 11 display the evolution of kinetic and potential energy, as defined by Equations (14a) and (14b), for the higher resolution Runs 25 and 27. There is a burst of turbulence associated with the nonlinear evolution of the Kelvin–Helmholtz instability: kinetic energy of the vertical shear is converted into gravitational potential energy as the heavier dust is lifted out of the gravitational potential well and mixed with the gas. However, once the layers reach new, thicker equilibria, the turbulence decays away and the flows again become laminar. The perfect dust-to-gas coupling prevents the dust from resettling back into thinner layers and there is no self-sustained turbulence.

In Figure 12(b), the Richardson number as a function of height is graphed for these same five runs. Because the Richardson number involves the ratio of two derivatives that both vanish at the midplane (which is especially exacerbated for noisy real data) it is not clear that the few points that have very low Richardson number near the midplane are not just numerical or spurious outliers. If we ignore those few points, then it appears that both of these runs result in minimum Richardson numbers right around

the canonical value of one-quarter. The final column of Table 1 shows the numerically computed minimum Richardson number for the cases where the dust layer was unstable. The lower resolution runs usually result in layers with minimum Richardson numbers that are slightly larger, in the 0.35–0.40 range, consistent with coarser mixing. If the resulting turbulence yields a new layer that is thicker than the critical thickness, the dust has no way to re-sediment because these simulations are in the limit of the perfect dust-to-gas coupling. In other words, one should not assume the final equilibria are marginally stable. In Figure 13, the final horizontally averaged dust-to-gas ratio for all the runs with unstable dust layers is plotted as a function of height. The axes are scaled in such a way so that profiles with the same minimum Richardson number coincide. The runs included in this figure include simulations with different global dust-to-gas ratios (Runs 10–18), different global gas radial pressure gradients (Runs 19–24), different layer widths, and different amounts of initial perturbations. Surprisingly, the vast majority of these simulations resulted in final dust layers with nearly the same minimum Richardson number, not much more than the classical critical value of one-quarter.

5. DISCUSSION AND FUTURE WORK

We revisited the case of no horizontal shear, both with and without the Coriolis force. The case without the Coriolis force is the most similar to classic Kelvin–Helmholtz instability, and the critical Richardson number for the onset of instability is close to the expected value of one-quarter, consistent with there being sufficient kinetic energy in the shear to lift the heavier fluid out of the gravitational well and mix it with the overlying lighter fluid (Garaud & Lin 2004). As first noted by Gomez & Ostriker (2005), the case with the Coriolis force is surprisingly different, with instability occurring at much higher Richardson numbers. However, the wavelengths of the most unstable eigenmodes for these thicker layers is smaller than the thickness of the layer itself. Ishitsu & Sekiya (2003) showed that the horizontal shear is able to eventually stabilize unstable eigenmodes by shearing them out to high wavenumber. However, unstable eigenmodes are able to grow for a period of time; the question is whether

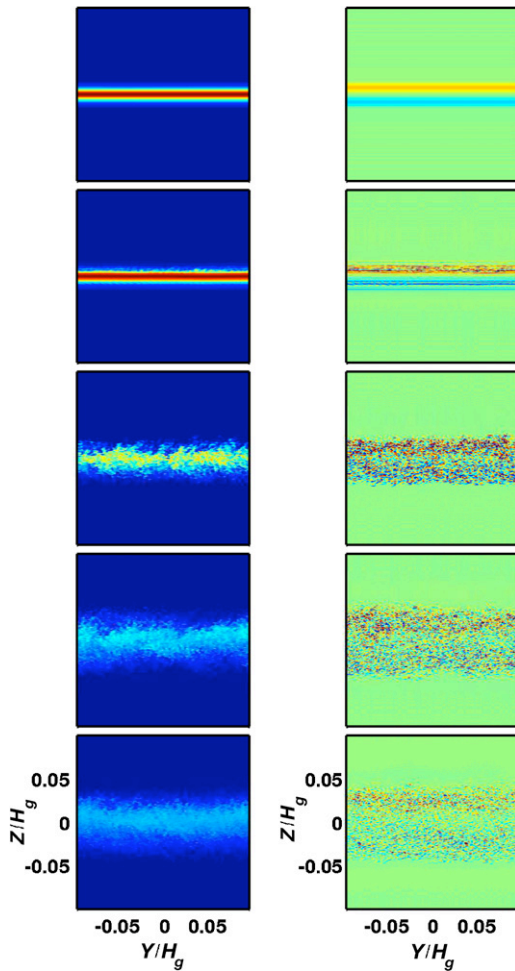


Figure 10. Three-dimensional nonlinear evolution of Kelvin–Helmholtz instability with Coriolis force and horizontal shear for Run 27. In this simulation, $\Sigma_d/\Sigma_g = 0.01$ and $\eta_0 V_{K0}/c_{s0} = 0.1$. The initial dust scale height is $H_d/H_g = 0.005$, corresponding to a peak local dust-to-gas ratio in the mid-plane of $\mu_0^\dagger = 2.0$, and a minimum Richardson number of $Ri_{\min} = 0.0169$. The amplitude of initial perturbations was $A_{\text{rms}} = 10^{-6}$. The panels show two-dimensional y – z ($\phi - z$) slices at $x = 0$ ($r = r_0$). The first column illustrates the evolution of the local dust-to-gas ratio μ (deep red = 2.0, deep blue = 0); the second column shows the evolution of the radial component of vorticity ω_x (red = vorticity that points into the page, blue = vorticity that points out of the page). The time interval between frames is 3.4 orbital periods.

(A color version of this figure is available in the online journal.)

they can grow to a large enough amplitude to trigger nonlinear effects and disrupt the dust layer before they are damped as they are sheared.

In order to investigate the competing influences of the Coriolis force (destabilizing) and horizontal shear (stabilizing), we used a three-dimensional spectral, anelastic, shearing-box code (Barranco & Marcus 2006) to simulate settled dust layers in the limit of perfect dust–gas coupling. We find that the stability of dust layers depends on the amplitude of initial perturbations: small perturbations grow for a period of time, but are damped before they reach sufficient magnitude to trigger nonlinear effects; whereas larger amplitude perturbations are able to grow to magnitudes that can disrupt the dust layer, resulting in turbulence and mixing. The Kelvin–Helmholtz instability in thicker layers has slower growth rates, implying that the magnitude of initial amplitudes would have to be larger. This was seen in Runs 6 and 7 in which the critical

threshold for perturbations was an order of magnitude larger for a layer that was 50% thicker. Thick dust layers that are stable according to the classic Richardson number criterion, but are unstable with the addition of the Coriolis force exhibit Kelvin–Helmholtz instability with very slow growth rates and at high spatial wavenumber (see Figure 5). Three-dimensional simulations of these layers indicate that the horizontal shear is able to damp the instability no matter how large the initial perturbations for these layers (see Runs 4 and 5). Thinner layers, on the other hand, have very fast growth rates, and the threshold amplitude is so low as to be practically irrelevant in real protoplanetary disks where there is no doubt fluctuations of such low magnitude.

In two-dimensional simulations of unstable dust layers, the turbulence that develops fills the computational domain and leads to large-scale mixing. Characteristic of “inverse cascades” in two-dimensional turbulence, small eddies merge with other eddies to form larger coherent vortices which chaotically advect the dust, homogenizing the dust-to-gas ratio. In three-dimensional simulations, the turbulence is locally confined to a region right around the original unstable dust layer and does not propagate through the rest of the computational domain. The unstable thin layers evolve to thicker, more stable layers with minimum Richardson numbers tantalizingly close to the value of one-quarter for the onset of instability in the absence of the Coriolis force and horizontal shear. These results hold when the global dust to gas ratio Σ_d/Σ_g and the global gas radial pressure gradient $\eta_0 V_{K0}/c_{s0}$ are varied. There is no reason to expect that the unstable layers in these simulations would evolve to a final state that just happens to be at the critical thickness for stability. One could imagine that the turbulence is so efficient at mixing that it results in layers whose widths are significantly thicker than thinnest stable layer. Because the simulations presented here are in the limit of the perfect dust-to-gas coupling, no further sedimentation of the dust is allowed so that the thicker final states cannot settle to the critical state.

Future work will involve two significant improvements. First, we will relax the perfect dust-to-gas coupling assumption and allow there to be a finite value for the stopping time. Dust will be treated as a second fluid with its own velocity field (Cuzzi et al. 1993). Layers that are unstable will develop turbulence and remix the dust with the gas, but then would be allowed to further settle. Johansen et al. (2006) performed two-dimensional simulations with Lagrangian particles embedded in the fluid and showed that layers evolved toward a self-regulated state in which further settling was inhibited by turbulence generated by Kelvin–Helmholtz instability, maintaining the layer in a dynamic equilibrium right at the critical thickness for instability. Like Gomez & Ostriker (2005), they found that the dust layers had very high critical Richardson numbers. Surprisingly however, they found the dust was not uniformly mixed in the saturated turbulent state, but was strongly clumped via a mechanism similar to the streaming instability of Youdin & Goodman (2005), which is only present if particles are allowed to slip through the gas. They suggested that such clumps might potentially be gravitationally unstable. Further works by Youdin & Johansen (2007); Johansen & Youdin (2007), and Johansen et al. (2007) have shown that despite Kelvin–Helmholtz instability, large boulders (meter scale) can settle, clump via the streaming instability, and potentially undergo gravitational collapse directly into kilometer-sized planetesimals. We plan to investigate these clumping phenomena with our higher resolution spectral simulations in the future.

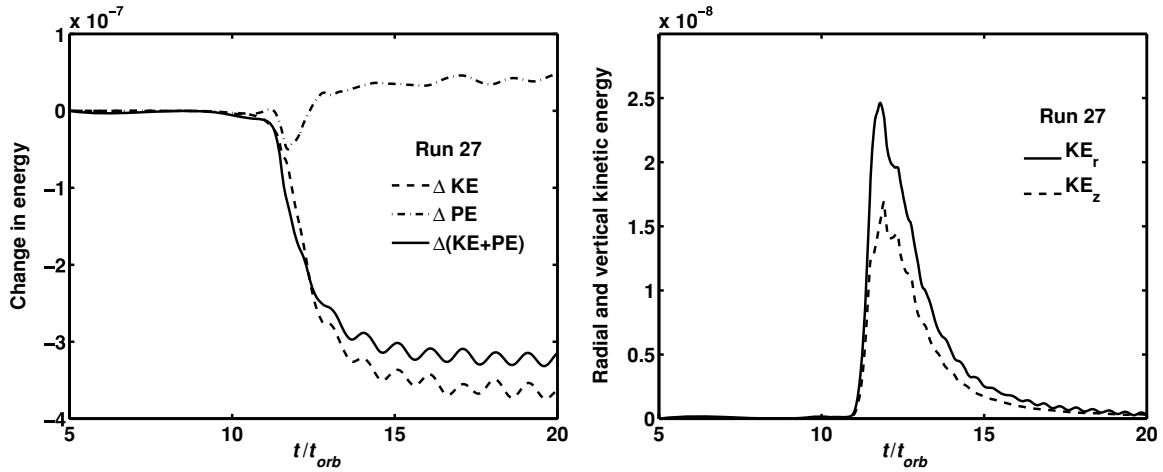


Figure 11. Evolution of energy for Run 27. In this simulation, $\Sigma_d/\Sigma_g = 0.01$ and $\eta_0 V_{K0}/c_{s0} = 0.1$. The initial dust scale height is $H_d/H_g = 0.005$, corresponding to a peak local dust-to-gas ratio in the midplane of $\mu_0^\dagger = 2.0$, and a minimum Richardson number of $Ri_{\min} = 0.0169$. The amplitude of initial perturbations was $A_{\text{rms}} = 10^{-6}$. The first column illustrates the evolution of the kinetic, potential, and total energies as functions of time; the second column shows the evolution of the radial and vertical components of the kinetic energy. There is a burst of turbulence associated with the nonlinear evolution of the Kelvin–Helmholtz instability: kinetic energy of the vertical shear is converted into gravitational potential energy as the heavier dust is lifted out of the gravitational potential well and mixed with the gas. However, once the layer reaches a new, thicker equilibrium, the turbulence decays away and the flow again becomes laminar.

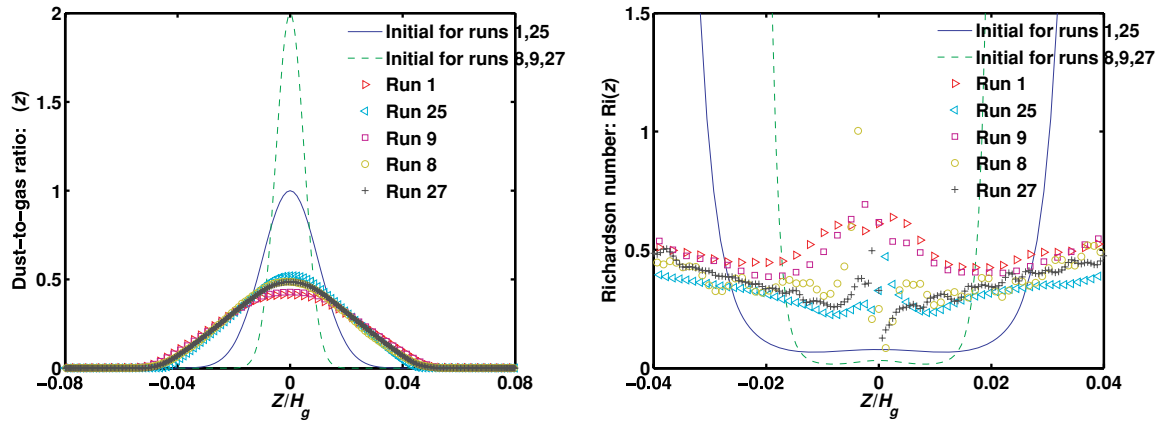


Figure 12. Horizontally averaged dust-to-gas ratio μ and Richardson number Ri as a function of height z for initial and final dust layers for Runs 1, 8, 9, 25, and 27. Runs 1 and 25 had similar parameters, except Run 25 had twice the resolution. Runs 9, 8, and 27 had similar parameters, except Run 8 had twice the resolution as 9, and Run 27 had twice the resolution as Run 8.

(A color version of this figure is available in the online journal.)

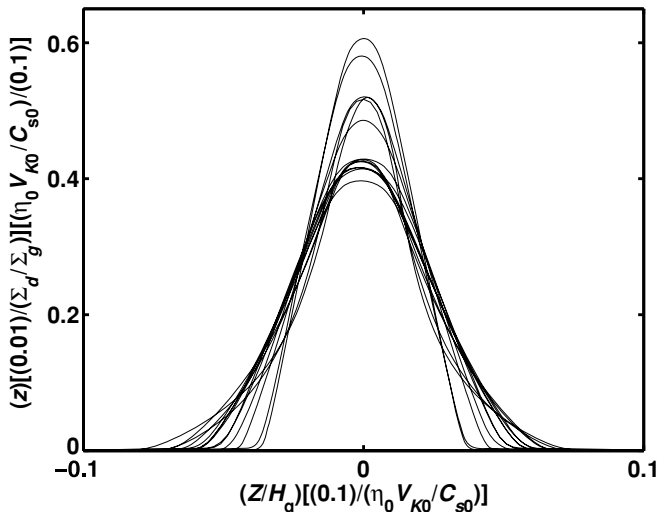


Figure 13. Horizontally averaged dust-to-gas ratio as a function of height for runs with unstable dust layers in Table 1. Axes are scaled in such a way so that layers that have the same Richardson number would lay on top of one another.

Second, we will add the effects of nonideal magnetohydrodynamics with finite resistance. Turner et al. (2007) investigated the magneto-rotational instability in protoplanetary disks with “dead zones” in the midplane where the ionization is too low to couple the fluid to the magnetic fields. However, they find that turbulence originating in the cosmic-ray-ionized surface layers can mix free charges into the interior and weakly couple the midplane gas to the magnetic fields, effectively eliminating the dead zone. Their analysis does not include the role that dust grains play in removing free charges and reducing the ionization. If turbulence lofts the particles throughout the disk, ionization can be suppressed, which will have the tendency to decouple the interior gas from the magnetic fields, allowing the dead zone to reform. Dust particle could then resettle, ionization could increase, recoupling the gas to the fields and generating a new phase of turbulence. We plan to investigate if there is indeed a limit cycle to the formation and destruction of the dead zone in protoplanetary disks.

The author thanks the National Science Foundation for support via the Astronomy & Astrophysics Postdoctoral Fellowship

program. Computations for this project were done at the Institute for Theory & Computation at the Harvard–Smithsonian Center for Astrophysics, and at the San Diego Supercomputing Center. The author also thanks Philip Marcus, Ramesh Narayan, and Niyash Ashfordi for fruitful conversations related to this project.

REFERENCES

- Adachi, I., Hayashi, C., & Nakazawa, K. 1976, *Prog. Theor. Phys.*, **56**, 1756
- Barranco, J., & Marcus, P. 2000, in *Studying Turbulence using Numerical Simulation Databases: Proc. 2000 Summer Program* (Stanford: Center for Turbulence Research), 97
- Barranco, J., & Marcus, P. 2005, *ApJ*, **623**, 1157
- Barranco, J., & Marcus, P. 2006, *J. Comput. Phys.*, **219**, 21
- Barranco, J., Marcus, P., & Umurhan, M. 2000, in *Studying Turbulence using Numerical Simulation Databases: Proc. 2000 Summer Program* (Stanford: Center for Turbulence Research), 85
- Beckwith, S., Henning, T., & Nakagawa, Y. 2000, in *Protostars and Planets 4*, ed. V. Mannings, A. Boss, & S. Russell (Tucson, AZ: Univ. of Arizona Press), 533
- Boyd, J. 2000, in *Chebyshev and Fourier Spectral Methods* (Mineola, NY: Dover)
- Brittain, S. D., Rettig, T. W., Simon, T., & Kulesa, C. 2005, *ApJ*, **626**, 283
- Cain, A., Ferziger, J., & Reynolds, W. 1984, *J. Comput. Phys.*, **56**, 272
- Canuto, C., Hussaini, M., Quarteroni, A., & Zang, T. 1988, in *Spectral Methods in Fluid Dynamics* (New York: Springer)
- Champney, J., Dobrovolskis, A., & Cuzzi, J. 1995, *Phys. Fluids*, **7**, 1703
- Chandrasekhar, S. 1960, *Proc. Natl Acad. Sci. USA*, **46**, 253
- Chandrasekhar, S. 1961, in *Hydrodynamic and Hydromagnetic Stability*, (New York: Dover)
- Cuzzi, J., Dobrovolskis, A., & Champney, J. 1993, *Icarus*, **106**, 102
- Dobrovolskis, A. R., Dacles-Mariani, J. S., & Cuzzi, J. N. 1999, *J. Geophys. Res.*, **104**, 30805
- Drazin, P., & Reid, W. 1981, in *Hydrodynamic Stability*, (Cambridge: Cambridge Univ. Press)
- Dullemond, C. P., Henning, T., Visser, R., Geers, V. C., van Dishoeck, E. F., & Pontoppidan, K. M. 2007, *A&A*, **473**, 457
- Frank, J., King, A., & Raine, D. 1985, in *Accretion Power in Astrophysics*, (Cambridge: Cambridge Univ. Press)
- Garaud, P., Barrière-Fouchet, L., & Lin, D. N. C. 2004, *ApJ*, **603**, 292
- Garaud, P., & Lin, D. 2004, *ApJ*, **608**, 1050
- Gilman, P., & Glatzmaier, G. 1981, *ApJS*, **45**, 335
- Glatzmaier, G., & Gilman, P. 1981a, *ApJS*, **45**, 351
- Glatzmaier, G., & Gilman, P. 1981b, *ApJS*, **45**, 381
- Goldreich, P., & Lynden-Bell, D. 1965, *MNRAS*, **130**, 125
- Goldreich, P., & Ward, W. 1973, *ApJ*, **183**, 1051
- Gomez, G., & Ostriker, E. 2005, *ApJ*, **630**, 1093
- Gottlieb, D., & Orszag, S. 1977, in *Numerical Analysis of Spectral Methods: Theory and Applications*, (Philadelphia, PA: Society for Industrial and Applied Mathematics)
- Gough, D. 1969, *J. Atmos. Sci.*, **26**, 448
- Ishitsu, N., & Sekiya, M. 2003, *Icarus*, **165**, 181
- Johansen, A., Henning, T., & Klahr, H. 2006, *ApJ*, **643**, 1219
- Johansen, A., Oishi, J. S., Low, M.-M. M., Klahr, H., Henning, T., & Youdin, A. 2007, *Nature*, **448**, 1022
- Johansen, A., & Youdin, A. 2007, *ApJ*, **662**, 627
- Kundu, P. 1990, in *Fluid Mech.*, (San Diego, CA: Academic)
- Lissauer, J. 1993, *ARA&A*, **31**, 129
- Marcus, P. 1986, in *Proceedings of Astrophysical Radiation Hydrodynamics*, ed. K.-H. Winkler, & M. Norman (Berlin: Springer) 359
- Marcus, P., & Press, W. 1977, *J. Fluid Mech.*, **79**, 525
- Ogura, Y., & Phillips, N. 1962, *J. Atmos. Sci.*, **19**, 73
- Pedlosky, J. 1979, in *Geophysical Fluid Dynamics*, (New York: Springer)
- Rettig, T., Brittain, S., Simon, T., Gibb, E., Balsara, D. S., Tilley, D. A., & Kulesa, C. 2006, *ApJ*, **646**, 342
- Rogallo, R. 1981, *Numerical Experiments in Homogeneous Turbulence*, Technical Memorandum 81315, NASA
- Ryu, D., & Goodman, J. 1992, *ApJ*, **388**, 438
- Safronov, V. S. 1969, in *Evolution of the Protoplanetary Cloud and the Formation of the Earth and Planets*, (Moscow: Nauka)
- Sekiya, M. 1998, *Icarus*, **133**, 298
- Sekiya, M., & Ishitsu, N. 2000, *Earth Planets Space*, **52**, 517
- Squire, H. 1933, *Proc. R. Soc. A*, **142**, 621
- Turner, N. J., Sano, T., & Dziourkevitch, N. 2007, *ApJ*, **659**, 729
- Weidenschilling, S. 1977, *MNRAS*, **180**, 57
- Weidenschilling, S. 1980, *Icarus*, **44**, 172
- Youdin, A., & Johansen, A. 2007, *ApJ*, **662**, 613
- Youdin, A., & Shu, F. 2002, *ApJ*, **580**, 494
- Youdin, A. N., & Chiang, E. I. 2004, *ApJ*, **601**, 1109
- Youdin, A. N., & Goodman, J. 2005, *ApJ*, **620**, 459